Deformation, annealing, reactive melt percolation, and seismic anisotropy in the lithospheric mantle beneath the southeastern Ethiopian rift: Constraints from mantle xenoliths from Mega

Andrea Tommasi, Virginie Baptiste, Alain Vauchez, Benjamin Holtzman

To cite this version:

Andrea Tommasi, Virginie Baptiste, Alain Vauchez, Benjamin Holtzman. Deformation, annealing, reactive melt percolation, and seismic anisotropy in the lithospheric mantle beneath the southeastern Ethiopian rift: Constraints from mantle xenoliths from Mega. Tectonophysics, 2016, 382, pp.186-205. 10.1016/j.tecto.2016.05.027 . hal-01355918

HAL Id: hal-01355918
https://hal.science/hal-01355918

Submitted on 28 Apr 2022

Deformation, annealing, reactive melt percolation, and seismic anisotropy in the lithospheric mantle beneath the southeastern Ethiopian rift: Constraints from mantle xenoliths from Mega

Andréa Tommasi [a,*], Virginie Baptiste [a], Alain Vauchez [a], Benjamin Holtzman [b]

[a] *Géosciences Montpellier, Université de Montpellier & CNRS, CC 60, Place E. Bataillon, 34095 Montpellier cedex 5, France*
[b] *Lamont–Doherty Earth Observatory, Columbia University, Palisades, NY, USA*

We explore the relations between deformation, annealing, and melt percolation during rifting and the effect of these processes on seismic anisotropy by analyzing the microstructures and crystal preferred orientations (CPO) in a suite of mantle xenoliths from Mega, in the southern end of the Ethiopian rift. Previous geochemical studies on these xenoliths showed evidence for interactions with variable melt types and volumes during the rifting process. The peridotites have dominantly coarse-porphyroclastic microstructures, but coarse granular or partially recrystallized microstructures also occur. The olivine CPO, characterized by orthorhombic to fiber-[100] patterns and moderate intensities, the common occurrence of (100) tilt walls, and the predominance of <0vw> rotation axes accommodating low angle misorientations in olivine support deformation by dislocation creep with dominant activation of the [100](010) system. Annealing (static recrystallization) of variable intensity followed this deformation. Modal enrichment in pyroxenes in >60% of the studied peridotites corroborates ex-tensive, but spatially heterogeneous reactive melt percolation leading to refertilization of the lithospheric mantle beneath the southern Ethiopian rift. The common interstitial shapes of the pyroxenes and lack of correlation be-tween the pyroxenes and the olivine CPOs in many samples suggest that part of the refertilization is post-kinematic. However, there is no simple relation between reactive melt percolation and annealing of the olivine deformation microstructure. Comparison with data from other xenolith localities points to changes in the meta-somatic imprint in the lithospheric mantle along the East African rift system correlated with the evolution in the rift maturity. Seismic properties averaged over all samples show typical lithospheric mantle patterns with fast propagation of P- and polarization of the fast S-waves parallel to the lineation. The anisotropy is moderate (<6% for P-waves and <4% for S-waves), implying that aligned melt must contribute to the strong seismic anisot-ropy measured in the Main Ethiopian rift, north of Mega.

1. Introduction

The East African rift is a natural laboratory for studying the continental rifting process at variable degrees of maturity, from initiation to oceanic accretion. The study of the evolution of surface deformation and magmatism in time and space (cf. review by Ebinger, 2012; Stamps et al., 2014), together with analysis of the topography (e.g., Ebinger et al., 1989), of the changes in rift morphology at large scale (e.g., Chorowicz, 2005), and of seismic tomography models (e.g., Pasyanos and Nyblade, 2007; Fishwick, 2010; Hansen et al., 2012; Civiero et al., 2015) indicate influence of both mantle plumes and pre-existing structures on the rift evolution. Seismic tomography also reveals a change in the lithosphere–asthenosphere boundary depth along the rift, consistent with the evolution in maturity of the system. In the Western rift and in the Tanzanian divergence, low seismic velocities are restricted to depths >100 km (Weeraratne et al., 2003). In contrast, beneath the Ethiopian and Kenyan segments of the rift, low velocity anomalies up to sub-Moho depths suggest extreme thinning of the lithospheric mantle in a rather narrow channel following the surface expression of the rift (Achauer and KRISP Teleseismic Working Group, 1994; Bastow et al., 2008; Hammond et al., 2013). This picture is corroborated by receiver function analysis, which shows a velocity increase at ~75 km depth correlated with the surface expression of the Ethiopian Rift and the Afars, interpreted as due to onset of decompression melting, and a velocity decrease at similar depths beneath the rift flanks, interpreted as the lithosphere–asthenosphere boundary (Rychert et al., 2012). In spite of their lower lateral

---

* Corresponding author.
E-mail address: andrea.tommasi@umontpellier.fr (A. Tommasi).

resolution, Rayleigh wave tomography models confirm this along-rift variation in the seismic structure of the uppermost mantle, with shallower low velocity anomalies in the northern part of the system (Pasyanos and Nyblade, 2007; Fishwick, 2010).

Despite all these data, the deformation of the lithospheric mantle in response to rifting remains poorly understood. Based on the assessment that the stresses needed to deform a 100 km-thick lithospheric plate at tectonic strain rates are higher than those produced by mantle convection (cf. calculations using the recent flow laws for the lithospheric mantle by Boioli et al., 2015), many studies proposed that magmatism plays a major role in rifting. Buck (2006) and Bialas et al. (2010) proposed that dyke intrusion might help in initiating rifting by heating up an initially thick and cold continental lithosphere. This model was further developed by Havlin et al. (2013), who proposed that repeated propagation of small-scale, cm-wide dykes from a melt accumulation layer at the lithosphere–asthenosphere boundary may progressively heat and thin the lithosphere at rates of a few km/Myr. The role of magmas in continental rifting may be even more subtle, as low melt fractions (< 1%) migrating through the lithospheric mantle might significantly decrease its viscosity (Takei and Holtzman, 2009). Reactive melt percolation may also change the composition of the lithospheric mantle (e.g., Le Roux et al., 2007) and cause heating (e.g., Havlin et al., 2013; Kourim et al., 2015), due to both heat advection and latent heat release by refertilization reactions. It may also reduce the mantle strength due to reaction-induced grain size reduction and phase mixing (e.g., Djikstra et al., 2002; Soustelle et al., 2010).

In the last decade, seismic studies have provided an increasing body of evidence for the presence of magmas within the lithospheric mantle beneath the East African rift. Seismic anisotropy data require the presence of oriented melt pockets in the crust and the mantle within the rift axis in Ethiopia and Afars (e.g., Kendall et al., 2005; Bastow et al., 2010; Hammond et al., 2014). Presence of melt at lithospheric depths has also been proposed in the younger western branch of the East African rift based on receiver function and seismic tomography data (Wölbern et al., 2012; Jakovlev et al., 2013). However, these data constrain neither the actual volumes nor the spatial distribution of the magmas. For instance, seismic anisotropy observations may be equally explained by alignment of small dykes or of melt films along grain boundaries. Moreover, seismic velocities and anisotropy depend on both the melt fraction and its spatial distribution and the two effects cannot be easily discriminated.

In the present study, we analyze textural evidence for deformation and melt percolation in mantle xenoliths from the southern end of the main Ethiopian rift (south of Mega in the Sidamo region, Fig. 1). Geochemical studies (Bedini, 1994; Bedini et al., 1997; Bedini and Bodinier, 1999; Lorand et al., 2003) pointed that these peridotites have recorded interactions with variable melt types and volumes in the lithospheric mantle. Bedini et al. (1997) identified two geochemical groups among these peridotites: (1) peridotites strongly enriched in LILE, with negative anomalies of HFSE, sometimes apatite-bearing, which they defined as "deformed", and (2) peridotites depleted or slightly enriched in LILE and devoid of any significant HFSE anomaly, which they defined as "granular". They interpreted the geochemical characteristics of "deformed" peridotites as resulting from interaction with small fractions of LILE-enriched melts saturated in Ti-oxides, while the "granular" peridotites were interpreted as recording re-equilibration with high fractions of basaltic melts. This interpretation was corroborated by the analysis of PGE abundances and sulfides modal compositions (Lorand et al., 2003). This xenolith suite is thus ideal to study the relations between reactive melt percolation (or metasomatism), deformation, and annealing and the consequences of these processes for the seismic properties of the lithospheric mantle.

After a short review of the geological evolution and of geophysical data in the region and the presentation of the methods, we describe in Section 4 the microstructural evidence for deformation, annealing, and reactive melt percolation in the Mega xenoliths and estimate the resulting seismic anisotropy. Section 5 presents insights on the relations and relative timing of deformation, annealing, and reactive melt percolation derived from these observations. It also compares the present data with compositional and microstructural data from mantle xenoliths from other localities within the East African rift system and with seismological data. This comparison allows discussing changes in deformation and magmatism and their relation to variations in the lithosphere–asthenosphere boundary depth along the rift. Finally we discuss the consequences of these processes for the seismic anisotropy beneath the Ethiopian rift.

2. Geological and geophysical background

The East African rift system extends over more than 4000 km, from the Afar triple junction to the Gulf of Mozambique (Fig. 1a). It is composed by a series of rifts at different stages of maturity, from incipient

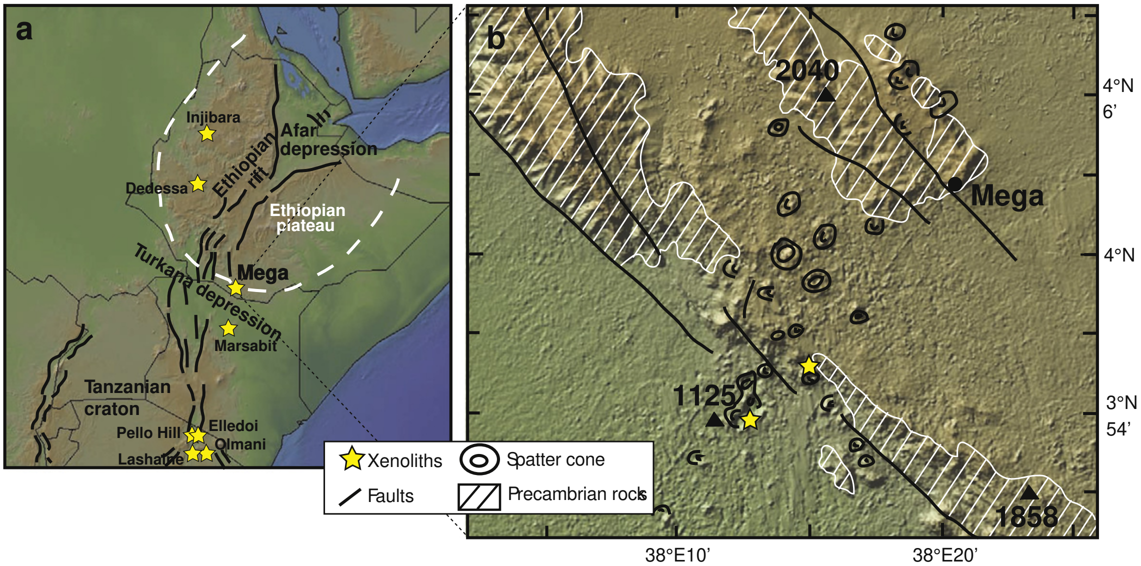

Fig. 1. (a) Digital topographic map (http://www.geomapapp.org, topography data from Ryan et al., 2009) of the East African rift system. Xenolith localities are indicated by stars. (b) Map of the Mega area, displaying the xenolith occurrences, as well as the rift-related faults, spatter cones, and Precambrian rocks outcrop domains (after Morten et al., 1992).

oceanization in the Afars to incipient rifting in Mozambique. The present study focuses on the eastern flank of the southern main Ethiopian rift, in the southern extremity of the Ethiopian plateau, just north of the Turkana Depression (Fig. 1b). The Turkana Depression is a 300 km wide system of extensional basins that connects the main Ethiopian rift to the Eastern (Gregory) rift in Kenya. This zone, which reactivates NE-trending Mesozoic rift structures (Bosworth, 1992), contains the earliest traces of volcanic activity (45–33 Ma) in the East African rift system (Ebinger et al., 2000). The surface expression of this early magmatism is offset to the northwest of the study area.

Extensive plume-related magmatism with a peak at 31–30 Ma lead to formation of the Ethiopian flood basalt province to the northwest of the study area, in northern Ethiopia and Yemen (Ebinger et al., 1993; Hofmann et al., 1997; Georges et al., 1998). Extension in Ethiopian rift started in the south, close to the study area, at ~22 Ma and progressed northwards (Woldegabriel et al., 1991; Ebinger et al., 1993). The Ethiopian rift records two additional volcanic episodes: extrusion of alkaline basalts and trachytes in the Miocene (19–11 Ma) and fissural volcanism accompanied by formation of cinder cones in the Plio-Pleistocene (Ebinger et al., 1993; Furman, 2007; Shinjo et al., 2011). In the study region (Fig. 1b), this latest magmatic event is expressed as lava flows and pyroclastic rocks with basanitic to nephelinitic compositions (i.e., products of low melting degrees), which carried abundant mantle xenoliths (Morten et al., 1992), among which are those studied here.

In contrast to other sectors of the East African rift system, the study region is poorly covered by seismological data. We have to rely on 'interpolating' between data obtained north and south of it: in the Main Ethiopian rift/Afars and in the Turkana depression/Kenyan rift. Crustal thickness data vary strongly between these two domains. The average crustal thickness beneath the plateau is ~38 km, whereas it is 25 ± 5 km in the Turkana depression; this variation may explain the difference in elevation between the two domains (Benoit et al., 2006). A detailed study of the seismic structure of the crust across the main Ethiopian rift also highlights a change in composition between the northwestern rift flank, where mafic underplating is important, and the southeastern flank, where felsic compositions dominate (Cornwell et al., 2010). If these data can be extrapolated ~500 km south, mafic underplating is not expected in the crust beneath Mega. Joint inversion of Rayleigh wave group velocities and receiver functions support lithospheric thicknesses of 70–80 km and maximum S-waves velocities of 4.3 km/s in the lithospheric mantle beneath the Ethiopian Plateau (Dugda et al., 2007). Thinner lithosphere (50 km) and lower maximum S-waves (4.1–4.2 km/s) were inferred beneath the central part of the main Ethiopian rift (Dugda et al., 2007). Low seismic velocities (Sn velocities of 4.1–4.3 km/s) were also inferred for the lithospheric mantle beneath the Turkana depression from Rayleigh wave dispersion modeling (Benoit et al., 2006). This data is consistent with predictions from continent-scale Rayleigh wave models, in which the Mega region is characterized by velocities of ~4.3 km/s in the shallow lithospheric mantle, crust with intermediate thickness between those observed in the Ethiopian plateau and in the Turkana depression, and a lithosphere-asthenosphere boundary at <80 km depth (Pasyanos and Nyblade, 2007; Fishwick, 2010). These models also indicate that the asthenosphere in this region has low shear wave velocities (−4% at 100 km depth and −2% at 200 km depth) relative to the ak135 reference Earth model.

SKS splitting studies in the northern and central main Ethiopian rift and in the Afars report coherent rift-parallel polarization of the fast S-wave, but variable delay times (0.5–1.7 s: Gashawbeza et al., 2004; 1–3 s: Kendall et al., 2005). Rift-parallel polarization of fast SKS and delay times of 0.8–2.4 s were also measured in southern Kenya and Tanzania (Gao et al., 1997; Walker et al., 2004; Bagley and Nyblade, 2013). High delay times (>2 s) beneath regions of recent volcanism and thinned lithosphere support an anisotropic signal dominated by oriented melt pockets (Kendall et al., 2005). This melt-related signal is probably superimposed to the anisotropy due to olivine crystal preferred orientations in the lithosphere and asthenosphere, which explains the similar fast S-wave polarization orientations but lower delay times in stations offset from volcanic centers (e.g., Gashawbeza et al., 2004). A more recent SKS study supports the existence of two anisotropic layers beneath Ethiopia: an upper layer with variable polarization directions beneath the plateau and the main rift, where anisotropy results from a combination of the effects of aligned melt pockets and fossil olivine crystal preferred orientations, and a lower anisotropic layer with a consistent NE–SW orientation that could be attributed to olivine crystal preferred orientations due to mantle flow from the African Superplume (Hammond et al., 2014). Based on numerical models, Hammond and Kendall (2016) even constrained spatial variations in the melt distribution. They proposed that, beneath the Main Ethiopian rift, melt is dominantly stored in vertically aligned disk-like inclusions, whereas it occurs in both horizontally and vertically aligned inclusions beneath the Red Sea.

3. Methods

3.1. Sample selection

We retrieved 42 xenoliths from the Morten et al. (1982) collection analyzed by Bedini (1994) and Bedini et al. (1997). When enough material was available, two thin sections were prepared in order to obtain a larger analyzed area. Because our observations and interpretations on sample microstructures differ from those by Bedini et al. (1997), we will refer in the following to their "deformed" peridotites as 'M1 peridotites', which represent the peridotites that interacted with small melt fractions, and to their "granular" peridotites as 'M2 peridotites', which represent the peridotites that interacted with larger volumes of basaltic melts. Among the samples selected for the present study, 9 are M1 peridotites, 10 are M2 peridotites. Three M1 peridotites (2 harzburgites and one lherzolite) and one M2 harzburgite from the Bedini et al. (1997) geochemical study could not be retrieved. In addition, we analyzed 13 peridotites and 10 pyroxenites from the same volcanic fields (Morten et al., 1992), for which no geochemical data is available. Tables 1 and 2 display the modal compositions, microstructures, metasomatism type, and thermobarometric data (when mineral compositions were available) for the studied samples. Table 1 also presents olivine CPO, grain size, and intragranular misorientation data for the peridotites and olivine-websterites.

3.2. Electron-backscattered diffraction (EBSD) data acquisition and treatment

Crystallographic preferred orientations (CPO) of olivine, pyroxenes, garnet, and spinel were measured at the SEM–EBSD facility at Geosciences Montpellier by indexing of electron back-scattered diffraction (EBSD) patterns produced by interaction of an incident electron beam with a carefully polished thin section tilted at 70° to the electron beam. Measurements were performed in a JEOL JSM 5600 scanning electron microscope using an acceleration voltage of 17 kV and a working distance of 23 mm. Maps covering almost entirely each thin section were obtained using steps between 15 and 50 μm, depending on grain size. Indexing rates ranged between 70 and 90%. Orthopyroxene and clinopyroxene were seldom misindexed for one another. Inaccurate mineral determination and misindexing due to olivine pseudo-symmetry were corrected by careful post-acquisition data treatment controlled by comparing EBSD maps and microscopic observations.

Modal compositions were approached as the area fraction occupied by each mineral on the EBSD maps. Comparison of data derived from the two sections of the same sample, when those were available, indicates some heterogeneity at the sample scale. However, in most cases, the present modal compositions are consistent within ±3% with those calculated based on chemical data (Bedini and Bodinier, 1999).

Crystal-preferred orientation data are displayed in pole figures, presented as lower hemisphere stereographic projections. To avoid over-

Table 1
Peridotites and olivine-websterite compositions, microstructures, thermometry, and olivine CPO, misorientation, and grain size data.

Sample	Thin section	Rock type	Microstructure[§]	Modal compositions (%)[#]					Metasomatism[*]		Mineral compositions[*]			Thermometry (°C)[*]		Olivine data			
				ol	opx	cpx	gt	sp	Type	Apatite	Mg$^{\#}$ ol	Mg$^{\#}$ opx	Mg$^{\#}$ cpx	Teq-c	Teq-b	J_ctf	BA_ctf	Mean M2M (°) [##]	Mean grain size (µm)[**]
ET35	ET35	Hz	C-Porph >20% rex	73	23	3	0	<1	M1		91.2	92.2	92.9	950	1026	3.51	0.62	2.13	1019.49
ET41	ET41	Lz	C-porph	78	14	7	0	1	M1	X	–	–	–	–	–	4.01	0.42	3.14	2092.58
ET46	ET46	Lz	CG	83	11	5	0	1	M1	X	90.9	91.6	92.1	1009	1029	5.75	0.48	2.18	1936.86
ET49	ET49	Hz	C-Porph	81	15	3	0	1	M1		91.2	92.02	92.91	954	972	3.18	0.56	2.34	1853.96
ET54	ET54	Hz	C-Porph	84	12	4	0	0	M1		91.5	92.18	93.41	901	923	7.79	0.62	2.65	2801.08
ET66	ET66A	Lz	C-Porph >50%rex	69	24	6	0	1	M1		–	–	–	–	–	2.76	0.58	1.54	931.94
	ET66B	Hz	C-Porph >50%rex	76	21	3	0	0	M1		–	–	–	–	–	2.06	0.44	1.63	973.11
ET69	ET69	Lz	C-Porph	50	32	16	0	2	M1	X	90.7	91.33	92.66	863	897	4.96	0.45	2.94	1485.14
ET83	ET83A	Hz	C-Porph	84	13	2	0	1	M1		–	–	–	–	–	5.74	0.58	3.19	2392.27
	ET83B	Hz	C-Porph	72	25	2	0	1	M1		–	–	–	–	–	5.01	0.50	3.47	2397.82
ET84	ET84A	Hz	C-Porph ~20% rex	86	11	3	0	0	M1	X	92.1	92.7	94.0	830	–	4.26	0.56	2.77	1632.29
	ET84B	Hz	C-Porph ~20% rex	76	22	1	0	1	M1	X	92.1	92.7	94.0	830	–	4.80	0.68	2.93	1671.13
ET32	ET32	Lz	C-Porph	46	36	16	0	2	M2		88.5	89.3	90.1	1049	–	3.93	0.39	4.38	1482.08
ET40	ET40	Lz	C-Porph	62	21	15	0	2	M2		–	–	–	–	–	3.16	0.71	2.78	1556.01
ET42	ET42	Lz	CG	75	17	7	0	1	M2		91.3	92.1	92.2	980	1010	5.26	0.55	1.86	2165.41
ET47	ET47	Hz	CG	70	26	3	0	<1	M2		88.4	89.8	89.2	1019	1020	3.51	0.58	1.98	1687.84
ET48	ET48A	Lz	C-Porph	52	26	20	0	2	M2		89.5	89.8	90.6	942	970	3.07	0.76	2.79	1798.56
	ET48B	Lz	C-Porph	56	29	14	0	1	M2		89.5	89.8	90.6	942	970	5.20	0.59	2.61	1838.90
ET70	ET70A	Lz	C-Porph	61	14	23	0	2	M2		–	–	–	–	–	4.14	0.57	3.70	2051.55
	ET70B	Lz	C-Porph	53	30	15	0	2	M2		–	–	–	–	–	5.02	0.51	3.71	2045.09
ET74	ET74A	Lz	M-Porph >50%rex	61	14	23	0	2	M2		90.9	91.6	92.6	916	941	3.08	0.43	1.45	1198.36
	ET74B	Lz	M-Porph >50%rex	64	16	19	0	1	M2		90.9	91.6	92.6	916	941	5.06	0.53	2.00	1390.30
ET75	ET75	Lz	MG	57	18	22	0	3	M2		89.5	90.2	90.8	1016	1043	3.26	0.53	1.03	1331.05
ET76	ET76	Lz	C-Porph	57	30	10	0	3	M2		89.5	90.3	91.3	933	971	3.56	0.79	3.68	2063.00
ET80	ET80	Lz	C-Porph	55	27	16	0	2	M2		89.3	90.0	91.1	925	936	2.97	0.29	2.88	1524.13
ET-VB1	ET-VB1	Hz	C-porph	79	17	3	0	1	no REE data		–	–	–	–	–	7.17	0.40	2.81	1566.66
ET30	ET30	Lz	C-porph	50	25	24	0	1	no REE data		–	–	–	–	–	6.08	0.57	3.39	1950.24
ET37	ET37	Lz	MG	52	20	27	0	1	no REE data		–	–	–	–	–	2.10	0.48	1.93	1178.08
ET38	ET38	Wehrl	C-Porph	78	0	21	0	1	no REE data		–	–	–	–	–	4.08	0.12	3.18	1690.82
ET51	ET51A	Lz	C-Porph	65	20	13	0	2	no REE data		–	–	–	–	–	3.00	0.39	2.25	1224.48
ET53	ET53	Lz	C-Porph	72	16	11	0	1	no REE data		90.2	90.9	91.5	969	995	4.72	0.69	2.96	2208.10
ET63	ET63	Lz	C-Porph	48	40	11	0	1	no REE data		–	–	–	–	–	3.88	0.34	3.47	1462.89
ET71	ET71	Lz	C-Porph	55	30	14	0	1	no REE data		–	–	–	–	–	6.01	0.25	2.94	1489.68
ET72	ET72	Hz	C-Porph	78	20	2	0	<1	no REE data		–	–	–	–	–	6.74	0.66	4.13	2205.16
ET73	ET73	Lz	C-Porph	61	19	17	0	3	no REE data		–	–	–	–	–	5.59	0.49	4.14	2718.03
ET82	ET82	Lz	C-Porph	62	20	17	0	1	no REE data		–	–	–	–	–	3.02	0.41	2.98	1656.64
ET85	ET85A	Lz	C-Porph	85	10	5	0	0	no REE data		–	–	–	–	–	6.50	0.50	3.34	2710.71
	ET85B	Lz	C-Porph	66	13	17	0	4	no REE data		–	–	–	–	–	9.86	0.69	4.10	3094.87
ET58	ET58	Ol-Wb	MG	27	42	26	0	5	no REE data		–	–	–	–	–	4.86	0.54	2.31	1016.42
ET65	ET65	Wb	CG	9	50	37	0	4	no REE data		–	–	–	–	–	4.98	0.16	1.56	803.56

[§] C-Porph = coarse-porphyroclastic; CG = coarse-granular; MG = medium-granular; rex = recrystallized.
[#] Modal compositions determined from EBSD maps.
[*] Based on data from Bedini (1994) and Bedini et al. (1997); equilibrium temperatures calculated using the Brey and Kohler (1990) two-pyroxene thermometer.
[##] M2M = misorientation relative to mean orientation of the crystal; average over the entire EBSD map.
[**] Apparent (2D) grain size estimated as the diameter of a circle with the same area as the grain; area weighted average over the entire EBSD map.

representation of large grains, data were reduced to one average crystallographic orientation per grain. When the foliation and lineation could be identified, the orientation of the main crystallographic directions: [100], [010] and [001] for olivine and pyroxenes, was plotted relative to the principal axes of the strain ellipsoid X, Y, and Z. When the foliation and lineation could not be identified in the hand samples, thin sections

Table 2
Pyroxenites data.

Sample	Thin section	Rock type	Microstructure[§]	Modal compositions (%)[#]					Mineral compositions[*]		Thermobarometry (°C/GPa)[*]			
				ol	opx	cpx	gt	sp	Mg$^{\#}$ opx	Mg$^{\#}$ cpx	Teq-core	Teq-rim	Peq-core	Peq-rim
ET55	ET55A	Wb	C-Porph	0	36	64	0	0						
	ET55B	Wb	C-Porph	0	14	86	0	0						
ET56	ET56	Gt-Wb	G	2	13	73	2	0	89	89.3	1156	1100	1.86	1.72
ET64B	ET64B	Wb	G	0	44	54	0	2						
ET68	ET58	Gt-Cpx	C-Porph	0	0	90	10	0						
ET77	ET77	Wb	C-Porph	0	42	58	0	0						
ET78	ET78	Gt-Cpx	C-Porph	0	<1	80	18	1						
ET81	ET81	Gt-Wb	G	0	36	53	10	1	90.3	91.5	764	775	0.86	0.91

[§] C-Porph = coarse-porphyroclastic; G = granular;.
[#] Modal compositions determined from EBSD maps.
[*] Based on data from Bedini (1994) and Bedini et al. (1997); calculated using the Brey and Kohler (1990) two-pyroxene thermometer and the Nickel and Green (1985) orthopyroxene-garnet barometer.

Table 3
Calculated seismic properties (ambient p,T conditions).

Sample	Thin section	Rock type	Microstructure[§]	Seismic properties (velocities in km/s and anisotropy in %)[*]												
				AVp	Vp max	Vp min	AVs pol max	AVs1	Vs1 max	Vs1 min	AVs2	Vs2 max	Vs2 min	AVp/Vs1	Vp/Vs1 max	Vp/Vs1 min
ET35	ET35	Hz	C-Porph >20% rex	7.55	8.68	8.04	4.93	2.94	4.97	4.83	3.82	4.86	4.68	6.52	1.78	1.66
ET41	ET41	Lz	C-porph	6.98	8.6	8.02	6.4	3.51	4.98	4.81	3.66	4.84	4.67	5.77	1.75	1.65
ET46	ET46	Lz	CG	10.46	8.84	7.96	6.64	3.84	5	4.81	5.79	4.88	4.61	8.79	1.79	1.64
ET49	ET49	Hz	C-Porph	6.75	8.62	8.06	4.87	2.4	4.93	4.82	3.5	4.86	4.69	4.98	1.75	1.67
ET54	ET54	Hz	C-Porph	12.34	8.95	7.91	7.95	4.52	5.07	4.84	5.94	4.87	4.59	11.37	1.82	1.63
ET66	ET66A	Lz	C-Porph >50%rex	5.63	8.56	8.1	3.64	1.62	4.92	4.84	3.43	4.86	4.69	5.7	1.76	1.66
	ET66B	Hz	C-Porph >50%rex	4.88	8.5	8.1	3.46	1.64	4.92	4.84	2.4	4.84	4.73	4.46	1.75	1.67
ET69	ET69	Lz	C-Porph	5.23	8.49	8.06	4.51	2.4	4.93	4.81	3.04	4.84	4.7	4.45	1.74	1.66
ET83	ET83A	Hz	C-Porph	11.43	8.9	7.93	7.41	3.98	5.03	4.83	6.07	4.89	4.6	9.7	1.8	1.64
	ET83B	Hz	C-Porph	7.28	8.61	8	5.65	2.37	4.95	4.83	3.55	4.84	4.67	5.15	1.74	1.65
ET84	ET84A	Hz	C-Porph ~20% rex	7.38	8.7	8.08	5.37	2.13	4.94	4.84	4.25	4.88	4.67	6.72	1.77	1.65
	ET84B	Hz	C-Porph ~20% rex	8.61	8.75	8.02	6.91	3.25	4.98	4.82	5.35	4.89	4.64	7.95	1.77	1.63
ET32	ET32	Lz	C-Porph	3.14	8.36	8.1	3.94	2.63	4.93	4.8	2.81	4.84	4.7	3.08	1.73	1.67
ET40	ET40	Lz	C-Porph	4.26	8.46	8.11	3.69	1.82	4.89	4.8	2.93	4.84	4.7	4.03	1.74	1.67
ET42	ET42	Lz	CG	8.83	8.74	8	5.72	2.98	4.97	4.82	4.73	4.87	4.65	7.78	1.78	1.64
ET47	ET47	Hz	CG	5.08	8.49	8.07	3.55	1.69	4.91	4.82	2.49	4.85	4.73	4	1.73	1.67
ET48	ET48A	Lz	C-Porph	4.71	8.48	8.09	2.9	1.8	4.88	4.8	2.62	4.83	4.71	4.4	1.75	1.67
	ET48B	Lz	C-Porph	5.44	8.52	8.07	4.92	2.54	4.94	4.82	2.94	4.84	4.7	5.38	1.75	1.66
ET70	ET70A	Lz	C-Porph	5.51	8.5	8.05	4.39	2.27	4.9	4.79	3.01	4.83	4.68	4.05	1.74	1.67
	ET70B	Lz	C-Porph	3.35	8.38	8.1	3.3	2.71	4.89	4.76	2.09	4.83	4.73	2.99	1.73	1.68
ET74	ET74A	Lz	M-Porph >50%rex	6.52	8.55	8.01	4.2	2.21	4.9	4.8	2.99	4.82	4.68	5.49	1.76	1.66
	ET74B	Lz	M-Porph >50%rex	8.54	8.67	7.96	5.37	2.07	4.94	4.84	4.17	4.85	4.65	7.91	1.78	1.64
ET75	ET75	Lz	MG	4.22	8.44	8.09	2.55	1.74	4.86	4.77	2.12	4.82	4.72	3.72	1.75	1.68
ET76	ET76	Lz	C-Porph	5.26	8.53	8.1	4.01	1.54	4.89	4.82	3.38	4.85	4.69	4.61	1.75	1.67
ET80	ET80	Lz	C-Porph	3.41	8.45	8.17	1.94	1.33	4.85	4.79	1.34	4.82	4.75	2.61	1.75	1.7
ET-VB1	ET-VB1	Hz	C-porph	12.23	8.88	7.85	8.29	5.77	5.06	4.78	5.28	4.86	4.61	8.84	1.79	1.64
ET30	ET30	Lz	C-porph	5.2	8.47	8.04	5	3.18	4.93	4.77	3.47	4.84	4.67	5.48	1.75	1.65
ET37	ET37	Lz	MG	2.41	8.33	8.13	2.28	1.16	4.85	4.79	1.64	4.81	4.73	2.75	1.73	1.69
ET38	ET38	Wehrl	C-Porph	6.53	8.49	7.96	4.41	4.13	4.94	4.74	1.04	4.76	4.71	3.85	1.74	1.67
ET51	ET51A	Lz	C-Porph	3.84	8.45	8.13	2.26	1.36	4.87	4.81	1.91	4.82	4.73	3.81	1.75	1.68
ET53	ET53	Lz	C-Porph	7.83	8.69	8.04	5.29	2.21	4.93	4.83	4.89	4.88	4.65	7.07	1.77	1.65
ET63	ET63	Lz	C-Porph	3.83	8.33	8.02	2.96	2.28	4.87	4.76	1.62	4.78	4.7	2.62	1.72	1.68
ET71	ET71	Lz	C-Porph	6.92	8.55	7.98	5.76	3.08	4.95	4.8	4.07	4.84	4.65	4.76	1.74	1.66
ET72	ET72	Hz	C-Porph	10.33	8.85	7.98	7.11	3.37	5.01	4.84	5.95	4.9	4.61	9.38	1.79	1.63
ET73	ET73	Lz	C-Porph	5.78	8.51	8.03	4.31	2.42	4.89	4.78	3.39	4.83	4.67	3.84	1.74	1.68
ET82	ET82	Lz	C-Porph	4.07	8.45	8.12	3.72	2.37	4.91	4.79	2.74	4.84	4.71	3.86	1.73	1.67
ET85	ET85A	Lz	C-Porph	10.6	8.82	7.93	7.73	4.82	5.06	4.82	4.45	4.85	4.64	9.79	1.8	1.64
	ET85B	Lz	C-Porph	6.44	8.56	8.03	5.76	3.63	4.96	4.78	3.59	4.82	4.65	7.25	1.78	1.65
ET58	ET58	Ol-Wb	MG	3.88	8.28	7.96	4.32	2.28	4.87	4.76	3.34	4.82	4.66	4.56	1.72	1.65
ET65	ET65	Wb	CG	3.06	8.22	7.97	2.52	1.77	4.84	4.76	1.88	4.79	4.7	3.06	1.72	1.66
ET55	ET55A	Wb	CP	8.46	7.90	4.26	0.08	4.13	4.92	4.72	3.50	4.82	4.66	7.62	1.76	1.63
ET64B	ET64B	Wb	CG	8.34	7.95	3.38	0.02	2.37	4.87	4.76	1.81	4.79	4.70	5.12	1.74	1.65
ET68	ET58	Gt-Cpx	CP	8.62	7.58	9.84	0.15	8.50	5.04	4.63	8.53	4.88	4.48	16.35	1.81	1.53
ET77	ET77	Wb	CP	8.38	7.85	4.93	0.13	4.01	4.91	4.72	3.49	4.83	4.67	6.30	1.73	1.63
ET81	ET81	Gt-Wb	CG	8.45	7.98	4.42	0.04	2.33	4.90	4.78	3.77	4.84	4.66	6.82	1.75	1.63

[§] C-Porph = coarse-porphyroclastic; CG = coarse-granular; MG = medium-granular; rex = recrystallized.
[*] Comparison between calculated and measured seismic velocities for a different rock types shows ≤ 5% of discrepancy (Barruol and Kern, 1996).

Table 4
Calculated seismic anisotropy for the average Mega sample considering different orientation of the foliation and lineation

Orientation of the foliation (S) and lineation (L)	Azimuthal anisotropy (horizontally propagating waves)			Polarisation anisotropy	
	Pn waves (%)	Love waves (%)	Rayleigh waves (%)	SKS (%)	Surface waves (Sh/Sv)[2]
S horizontal / L horizontal	3.4	0.5	2.0	2.0	1.1
S vertical / L horizontal	5.1	1.3	2.4	3.3	1.0
S vertical / L vertical	1.7	1.3	1.3	1.3	1.0
S dipping by 45° / L horizontal	5.1	1.7	2	2.4	1.0
S dipping by 45° / L downdip	3.2	2.4	3.8	2.9	1.0

were cut in random orientations. However, all samples showed a well-defined olivine CPO, indicating deformation by dislocation creep with dominant activation of the [100](010) slip system. To facilitate comparison between different samples, we present therefore the CPO data of all samples rotated into a common orientation, in which the maximum concentration of olivine [100] and [010] axes are parallel to the E–W and the N–S directions of the pole figure, respectively.

The strength of the olivine CPO was quantified using the dimensionless J-index, which is the volume-averaged integral of squared orientation densities (Bunge, 1982). The J-index was calculated using the MTEX toolbox in Matlab (http://mtex.googlecode.com; Hielscher and Schaeben, 2008; Bachmann et al., 2011) with orientation distribution functions (ODF) calculated using a "de la Vallée Poussin" kernel with a halfwidth of 10°. This calculation was performed using both one-orientation datum per pixel and the mean orientation of each grain. The former choice allows relating the CPO strength to the variations in grain size. Large crystals contribute more to the J-index, as they do for the anisotropy of physical properties. In naturally deformed peridotites, the J-index, when calculated using the same parameters as in this study, ranges between 1 (random CPO) and 18, with an average at ~4.8 (Tommasi and Vauchez, 2015).

The olivine CPO symmetry is characterized by the dimensionless BA-index (Mainprice et al., 2014) defined as:

$$BA\ index = {}^{1}/_{2}\left(2-\left(\frac{P010}{G010+P010}\right)-\left(\frac{G100}{G100+P100}\right)\right) \quad (1)$$

where P and G are indexes used to characterize the shape of the distribution (P for Point and G for Girdle; Vollmer, 1990) of the olivine principal axes ([100], [010] and [001]). These indexes are calculated from the eigenvalues of the normalized orientation matrix as $P = \lambda_1 - \lambda_3$ and $G = 2(\lambda_2 - \lambda_3)$ using the MTEX texture analysis Matlab toolbox. The BA-index allows a classification of the olivine CPO symmetry into 3 types: fiber-[010], characterized by a point concentration of [010] and a girdle distribution of [100] (BA-index < 0.35), orthorhombic, characterized by point concentrations of both [100] and [010] (0.35 < BA-index < 0.65), and fiber-[100], characterized by a point concentration of [100] and a girdle distribution of [010] (BA-index > 0.65).

The automatic grain detection routine in the MTEX toolbox (Bachmann et al., 2010) is used for quantitative analysis of grain sizes and shapes. Grain boundaries are defined by misorientations between neighboring pixels >15°. Intracrystalline orientation gradients, which are a proxy for the dislocation density, were quantified by the analysis of the misorientation of each pixel relative to the average orientation of the grain (M2M). The decrease in the mean M2M value (averaged over the entire sample) is used as a proxy for quantifying the recrystallization degree of the sample. Both dynamic and static (annealing) recrystallization should result in decrease of the intracrystalline dislocation density due to recovery, increase of the volume (area in a 2D EBSD map) occupied by recrystallized grains, which have low dislocation densities, and/or growth of grains with low dislocation densities.

3.3. Seismic properties

Seismic properties were calculated using the CPO of all major phases and their respective modal content estimated from EBSD maps (Mainprice, 1990). Olivine, orthopyroxene, clinopyroxene, garnet, and spinel single-crystal elastic constant tensors at ambient conditions were used (Hearmon, 1984; Abramson et al., 1997; Chai et al., 1997a, b; Collins and Brown, 1998). A Voigt–Reuss–Hill averaging was applied in all calculations. Average seismic properties for the lithospheric mantle beneath Mega were calculated by averaging the elastic constant tensors of all samples calculated using the CPO data rotated into a common structural reference frame, that is, considering a geographically coherent orientation of the foliation and lineation for all samples. These values represent therefore maximum estimates of the seismic anisotropy that may be produced by the studied xenolith suite.

4. Results

4.1. Modal compositions and thermobarometry

M1 peridotites are mainly harzburgites and M2 peridotites are dominantly lherzolites (Fig. 2 and Table 1). There were a few more lherzolites within M1 peridotites in the original Bedini et al. (1997) dataset, but comparison of the average compositions of each group in the present study (M1: 75% ol, 19% opx, 5% cpx, 1% sp. and M2: 59% ol, 23% opx, 16% cpx, 2% sp) and in Bedini et al. (1997) (M1: 73% ol, 20% opx, 6% cpx, 1% sp and M2: 65% ol, 21% opx, 13% cpx, 2% sp) corroborates the representativity of the present dataset. Clinopyroxene-rich lherzolites predominate among the peridotites for which no REE data is available (Fig. 2), but this group also contains two harzburgites (ET72, ETVB1), an orthopyroxene-rich lherzolite (ET67), and one wehrlite (ET38). The pyroxenites have a wide variety of compositions (Fig. 2a and Table 1). Three are olivine-websterites with olivine contents ranging from 27 to 8%. Six are websterites (four spinel-bearing and two garnet-bearing, among which one with 2% olivine) and the last one is a garnet clinopyroxenite.

Comparison of the modal compositions with the compositional evolution predicted by different melting models (Fig. 2b) highlights that most M1 peridotites have compositions consistent with predictions by partial melting models, except for a few outliers, which are slightly enriched in clinopyroxene or in olivine. In contrast, most M2 peridotites are enriched in clinopyroxene or in both clino- and orthopyroxene.

The contrast in modal compositions between M1 and M2 peridotites is associated in most cases with coherent changes in mineral chemistry. M1 peridotites tend to display higher olivine Mg# (atomic Mg / (Fe + Mg)), ranging between 0.907 and 0.921. Olivine Mg# in M2 peridotites varies between 0.884 and 0.913. Ortho- and clinopyroxene Mg# is also higher in M1 peridotites (Table 1). However, some samples have mineral compositions inconsistent with their modal data. For instance, M2 harzburgite ET47 has Fe-rich olivine (Mg# 0.884), but a refractory modal composition (Fig. 2b), while M1 lherzolite ET69 has Mg-rich olivine (Mg# 0.907), but a fertile modal composition (50% olivine, Table 1).

Equilibration temperatures calculated using post-exsolution pyroxene compositions measured by Bedini (1994) and the two-pyroxene geothermometer of Brey and Köhler (1990; uncertainty of ±50 °C) range between 830 and 1049 °C (Table 1). Rim temperatures are in general higher than core ones, suggesting heating (Fig. 3 and Table 1). The lowest temperatures (<900 °C) are observed in M1 peridotites cores and the highest temperatures, in M2 peridotites. The latter also show a smaller dispersion of equilibrium temperatures. For the two garnet-bearing pyroxenites, equilibration pressures and temperatures were calculated using the barometer of Nickel and Green (1985) and the two-pyroxene geothermometer of Brey and Köhler (1990), respectively. Olivine-bearing garnet-websterite ET56 yields equilibration conditions of 1156 °C and 1.86 GPa (ca. 60–65 km depth) based on core compositions and of 1100 °C and 1.72 GPa based on rim compositions. Olivine-free garnet-websterite ET81 yields abnormal low pressures and temperatures: 775 °C and 0.9 GPa (ca. 30–35 km depth, well outside the stability field of garnet) using both core and rim compositions.

4.2. Microstructures

4.2.1. Peridotites

Bedini et al. (1997) proposed a simple correlation between microstructural types and chemical composition of the Mega peridotites, implying a relationship between the deformation and the melt migration histories. However, the present analysis of the microstructures, which is based on association of optical observations with data derived from EBSD mapping, does not corroborate this correlation. Coarse-porphyroclastic microstructures prevail in all geochemical groups. This microstructure is characterized by predominance of plurimillimetric olivine crystals with a well-developed substructure (subgrains and undulose extinction; Fig. 4a–d), indicative of deformation under low stress (probably high temperature) conditions. Some samples from the three groups (ET42, ET46, ET47, ET75, ET37) show medium to coarse granular microstructures (Fig. 4f) characterized by a lower density of intracrystalline deformation features in olivine, which implies that deformation was followed by effective annealing. Finally, a few peridotites from both M1 and M2 groups (ET35, ET66, ET84, ET74) display a partially recrystallized microstructure, characterized by variable proportions of small olivine crystals with polygonal shapes and very low internal misorientations, which growth at the expenses of an initially coarse porphyroclastic microstructure (Fig. 4e).

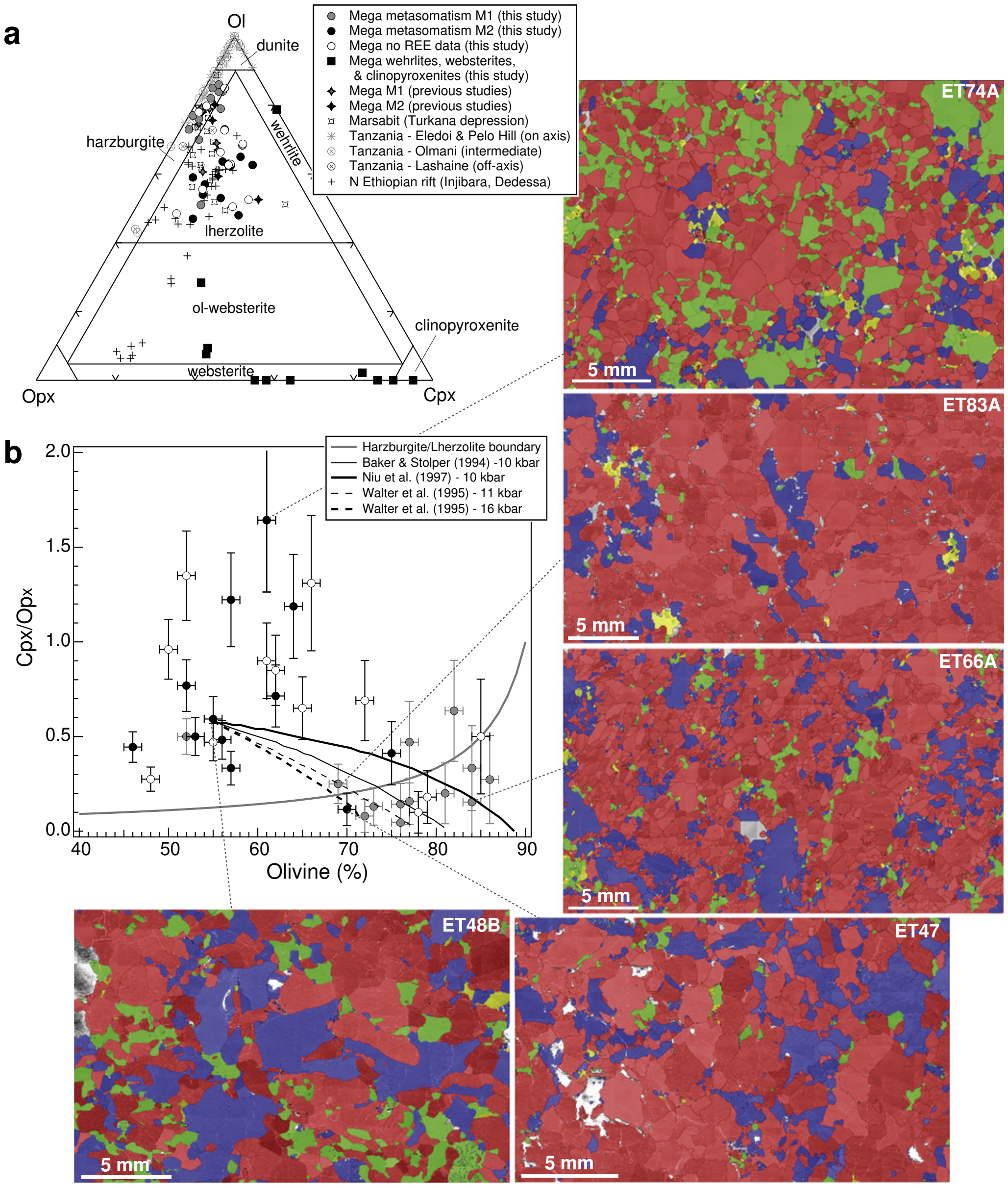

Fig. 2. Modal compositions. (a) Ternary olivine–orthopyroxene–clinopyroxene diagram comparing the modal compositions of the studied xenoliths as a function of the metasomatism type as defined by Bedini et al. (1997) with those from other xenolith localities in the East African Rift System (data from Kaeser et al., 2006; Beccaluva et al., 2011; Baptiste et al., 2015). (b) Modal compositions of the studied Mega harzburgites and lherzolites plotted on a clinopyroxene/orthopyroxene vs. olivine diagram for comparison with isobaric melting models calculated for an initial modal composition of 55% olivine, 28% opx, 15% cpx and 2% spinel. The spatial distribution of the three mineral phases and the shape of the phase boundaries are illustrated by EBSD phase maps (red = olivine; blue = orthopyroxene; green = clinopyroxene) of some representative samples.

Average apparent grain sizes of olivine (diameter of equivalent spheres with the same area as the grains, weighted by the grain area in the EBSD map) in the peridotites range from 0.9 to 3.1 mm (Fig. 5). In the coarse porphyroclastic peridotites, olivine crystals usually display irregular shapes. Clear shape preferred orientations, marking a foliation, are seldom observed. The exception is ETVB1 (Fig. 4d), which shows a foliation marked by the alignment of tabular olivine crystals. Subgrain boundary spacing in olivine varies from sample to sample. Subgrain boundaries are closely spaced and undulose extinction is common in ET32 (Fig. 6a), whereas ETBV1 is characterized by widely spaced subgrain boundaries (Fig. 6b). Harzburgite M1 ET72 exhibits an intermediate microstructure, with common, but well-defined and widely spaced subgrain boundaries (Fig. 6c). The decrease in density of intracrystalline deformation features records either deformation under lower stress (probably higher temperature) conditions or annealing. It may be quantified by the analysis of the average (over all olivine crystals in the EBSD map) misorientation relative to the mean orientation of the grain (M2M). Closely spaced subgrain boundaries and undulose extinction result in high average M2M value, which is of 4.4° for ET32, 4.1° for ET72, but only 2.8° for ETVB1 (Fig. 5 and Table 1). Olivine-olivine grain boundary shapes also vary. They range from serrated or sinuous, that is, showing small or large wavelength sinuosity (Fig. 6a, c), to polygonal, leading to 120° triple junctions (Fig. 6b). All gradations between the above microstructures are observed among the studied peridotites. A striking feature of the peridotite suite is that the decrease in the intragranular misorientation is not systematically correlated with a reduction in the sinuosity of grain boundaries. For instance, coarse-granular M2 harzburgite ET42 displays olivine crystals with low intragranular misorientations (average M2M = 1.9°), but curvilinear grain boundaries (Fig. 4f). In contrast, coarse-porphyroclastic

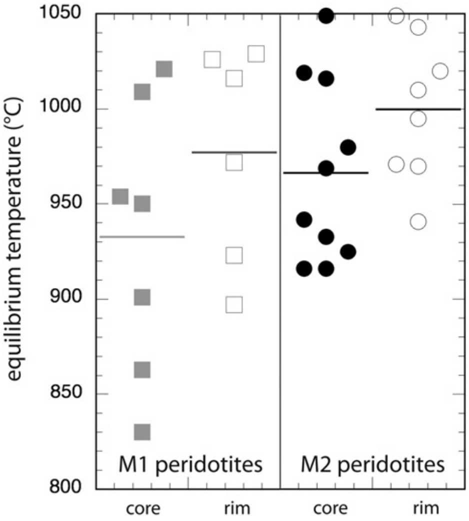

Fig. 3. Average core and rim equilibrium temperatures of some M1 and M2 peridotites estimated using the Brey and Kohler (1990) two-pyroxene geothermometer (uncertainty of 50 °C) and the post-exsolution pyroxene compositions measured by Bedini (1994). The bar marks the average equilibrium temperature for each category.

harzburgite ETVB1 has olivine crystals with well-developed subgrain boundaries (average M2M = 2.8°), but straight grain boundaries (Figs. 4d and 6d).

Partially recrystallized peridotites differ from each other essentially in the proportion of recrystallized grains, which attains >50% in M1 harzburgite ET66 and in M2 lherzolite ET74. Average recrystallized olivine sizes range from 380–500 μm in ET35, ET66, and ET74 to >600 μm in ET84. In ET66 and ET84, recrystallized grains have tabular shapes and a shape preferred orientation (Figs. 4e and 6d, e). In ET66, the elongation of the recrystallized grains is subparallel to a compositional banding marked by enrichment in clino- and orthopyroxene (Fig. 2). However, none of the partially recrystallized samples shows a clear planar or anastomosed arrangement of the recrystallized grains. The latter are either distributed randomly within the sample or form irregularly shaped patches (Figs. 4e and 6d, e). It is noteworthy that the olivine neoblasts replace both deformed olivine (Fig. 6d) and orthopyroxene porphyroclasts (Fig. 6e); this suggests that olivine neoblasts may have formed both by recrystallization (nucleation of a new crystal at the expenses of a deformed olivine crystal aiming to reduce the elastic energy associated with the dislocations) and by crystallization in response to the reaction between the peridotite and Si-poor melt (dunitization reaction). Partially recrystallized and granular peridotites may be discriminated from the coarse porphyroclastic peridotites by their lower

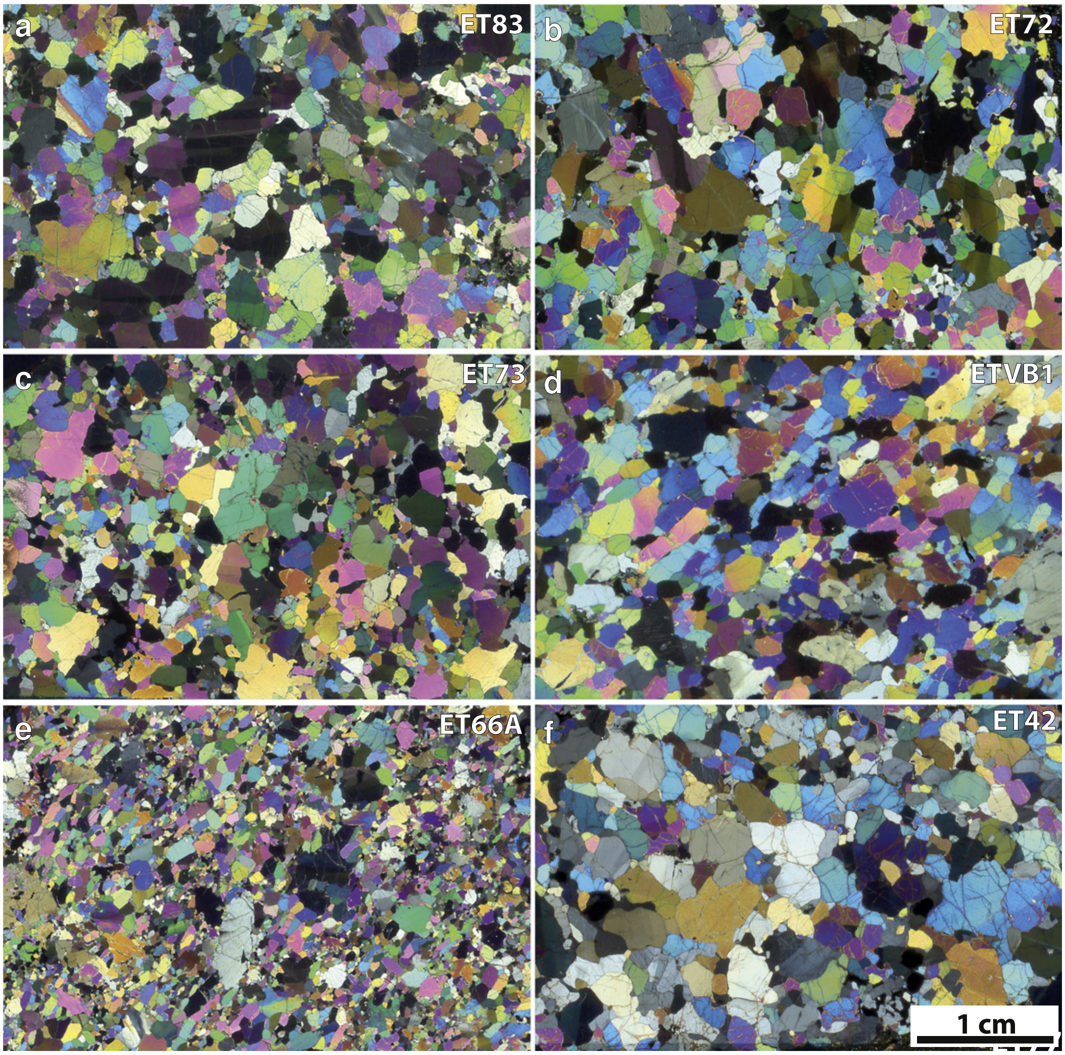

Fig. 4. Full-size thin section photomicrographs in plane-polarized light showing the typical microstructures of Mega peridotites: (a–d) Coarse porphyroclastic peridotites displaying increasing degrees of annealing; (e) partially-recrystallized peridotite; (f) coarse-granular peridotite. Scale bar is the same for all pictures.

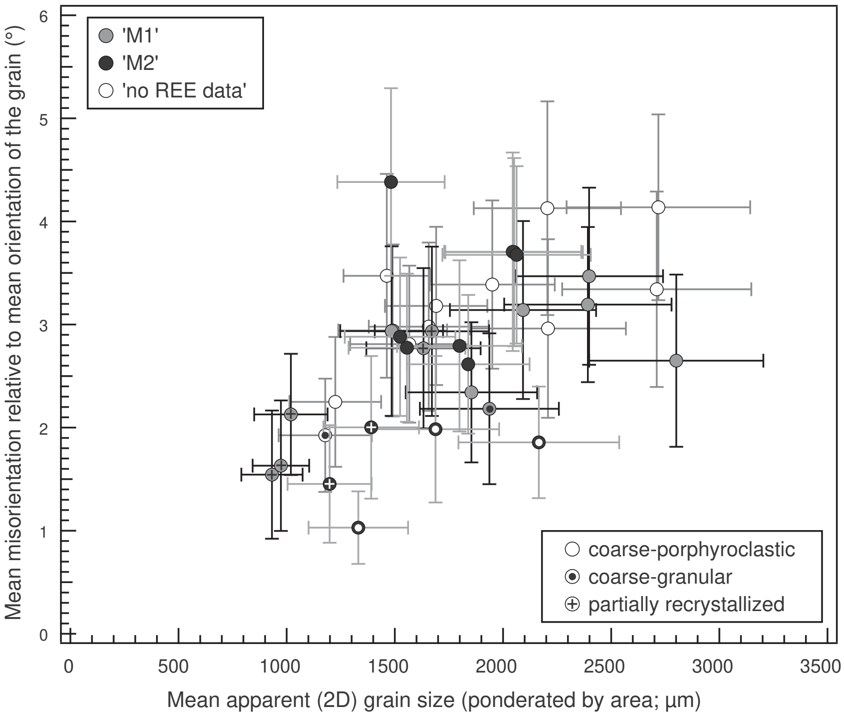

Fig. 5. Mean apparent (2D) grain size vs. the mean intragranular misorientation (M2M); both values are area-weighted averages at the thin section scale. Error bars indicate standard deviations. Dotted symbols indicate coarse-granular peridotites, crossed ones, partially recrystallized peridotites; all other samples are coarse-porphyroclastic peridotites with variable degrees of annealing. As expected, recrystallization and annealing result in low average M2M values; among coarse-granular and partially recrystallized peridotites M2M values >2.2 are only observed for sample ET84, which has a low recrystallized volume (~20%).

average M2M (usually <2.2°, Fig. 5), since this value decreases with both the increase of the recrystallized area fraction and the recovery of the dislocation microstructure. The slightly higher average M2M (2.8–2.9°) of M1 harzburgite ET84 reflects its low recrystallized fraction (~20%).

In all peridotites, independently of the microstructure defined by the olivine deformation or of the geochemical group, ortho- and clinopyroxene have very irregular shapes and no shape-preferred orientation (Figs. 2, 4, and 6). Orthopyroxene occurs mainly as isolated grains with highly variable sizes, but it may also form aggregates with clinopyroxene and spinel. Orthopyroxene-spinel symplectites are rare. Large, plurimillimetric orthopyroxene crystals usually display well-defined kink bands and undulose extinctions (Figs. 4a, f, 6f). They often contain olivine inclusions and have interpenetrating boundaries with olivine (Fig. 6a, e, f). Smaller orthopyroxene grains (0.4–1 mm) usually do not show intracrystalline deformation features. Both large and small orthopyroxene crystals commonly display cuspate terminations at olivine-olivine-opx triple junctions (Fig. 6g, h). Small crystals often have interstitial or film-like shapes (Fig. 6e). A particular feature of partially recrystallized peridotites is the presence, in coarse orthopyroxene crystals, of embayments filled by olivine (Fig. 6e). In most peridotites, orthopyroxene contains exsolutions (Figs. 4b–d, 6c, f). Exsolutions are not observed optically in ET32 (Fig. 6a), ET35, ET37, ET42 (Fig. 4f), ET46, ET47, ET63, and ET75, consistently with the high equilibrium temperatures calculated for most of these peridotites (Table 1).

Clinopyroxene tends to display slightly smaller sizes (0.3–3 mm) than orthopyroxene, but the largest crystals in clinopyroxene-rich lherzolites may attain up to 5 mm in diameter (Figs. 2 and 4). It occurs either as dispersed crystals with very irregular, interstitial-like shapes or in aggregates with orthopyroxene (Fig. 2). Large clinopyroxene crystals often contain olivine inclusions. Exsolutions of orthopyroxene are observed in many samples. Wehrlite ET38 has a particular texture, characterized by poikilitic clinopyroxenes up to 4 mm wide enclosing smaller olivine crystals. It is noteworthy that the different fragments of olivine enclosed in these poikilitic pyroxenes preserve the same crystallographic orientation, implying a static replacement reaction. Clinopyroxene crystals usually show no intracrystalline deformation features, but in some samples undulose extinction is present.

4.2.2. *Pyroxenites*

Websterites and clinopyroxenites microstructures range from granular (ET64, ET81) (Fig. 7a) to coarse-porphyroclastic (ET55, ET56, ET68, ET77, ET78; Fig. 7b). In the granular websterites, plurimillimetric clinopyroxene and orthopyroxene crystals often display polygonal boundaries and exsolutions. In the porphyroclastic websterites, millimetric to centimetric anhedral porphyroclasts of clinopyroxene containing exsolutions can be observed. They sometimes exhibit undulose extinctions as well as kink bands. Smaller crystals tend to display polygonal boundaries and are devoid of intracrystalline deformation features. In ET56, ET68, ET78, and ET81, garnet crystals are partially kelyphitized and have millimetric sizes (Fig. 7b). In garnet websterite ET81, garnet occurs as small grains along both ortho- and clinopyroxene grain boundaries, while in garnet-clinopyroxenites ET68 and ET78, garnet occurs both as dispersed crystals with interstitial shapes and enclosed within coarse clinopyroxene crystals showing undulose extinction. In garnet-websterite ET56 garnet occurs essentially along exsolution lamellae within coarse clinopyroxene crystals and as inclusions in a deformed olivine crystal that partially replaces clinopyroxene. Olivine-websterites show irregularly shaped olivine crystals with subgrains and undulose extinction (former coarse-porphyroclastic microstructure) partially replaced by orthopyroxene-rich or clinopyroxene-rich aggregates. In ET58, large crystals with irregular shapes and undulose extinction compose the former, whereas the latter are formed by small (<1 mm) crystals with a granular microstructure. In ET65, deformed olivines are enclosed in a websteritic matrix composed by large orthopyroxene crystals with frequent kinks, and by smaller, irregularly shaped clinopyroxenes and orthopyroxenes.

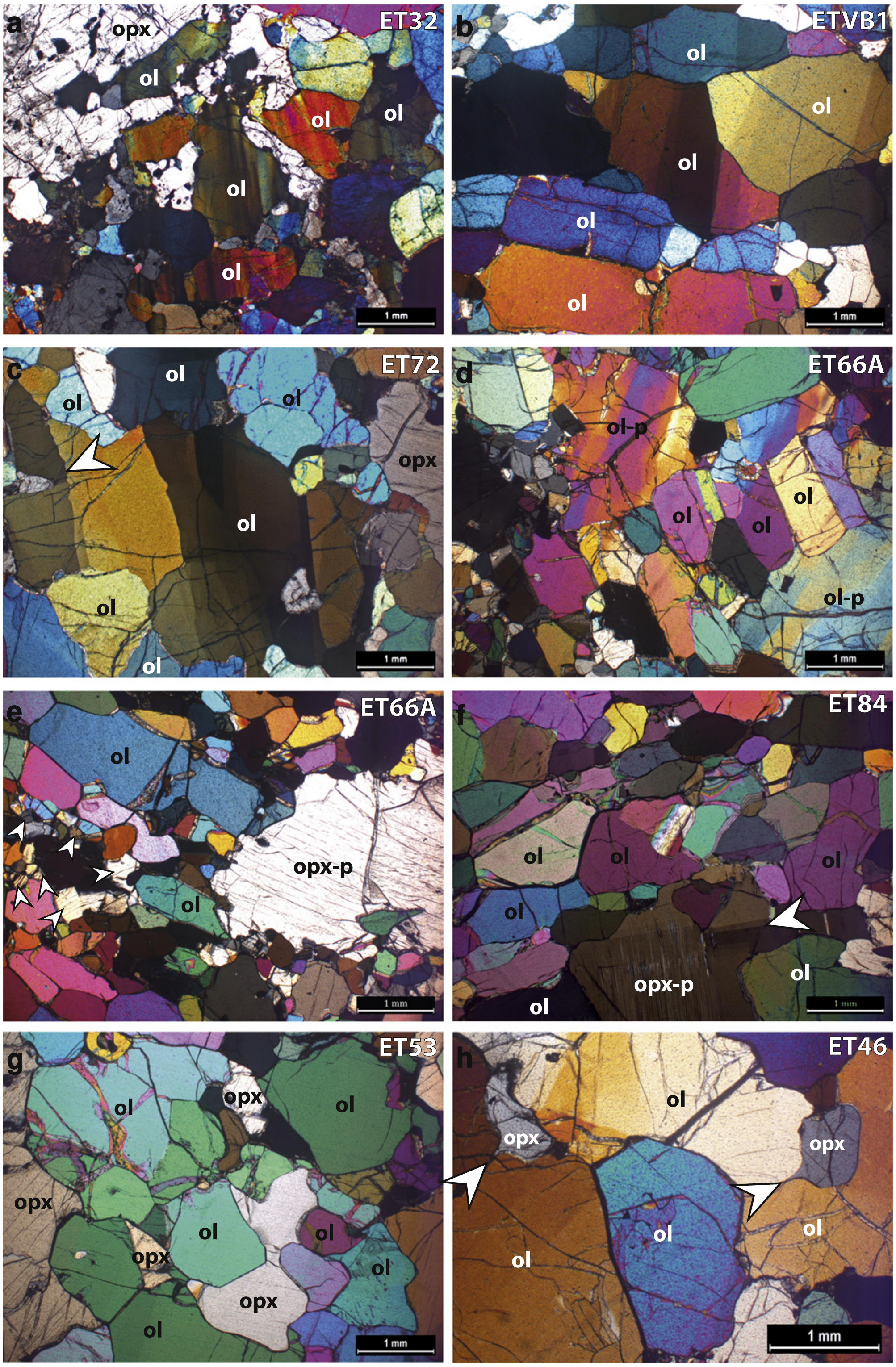

Fig. 6. Photomicrographs in plane-polarized light. (a) Coarse-porphyroclastic M2 lherzolite ET32 showing olivine porphyroclasts with closely spaced subgrain boundaries and undulose extinction (ol) partially replaced by a coarse orthopyroxene crystal (opx) with a very irregular shape and numerous olivine inclusions. (b) Coarse-porphyroclastic harzburgite ETVB1 exhibiting elongated olivine crystals (ol) with widely spaced subgrain boundaries and polygonal grain boundaries. (c) Coarse-porphyroclastic harzburgite ET72 showing olivine crystals (ol) with well developed subgrain boundaries and very sinuous grain boundaries, recording grain boundary migration; the arrow marks a sutured subgrain boundary, which shape suggests migration. (d) Partially recrystallized M1 harzburgite ET66 displaying tabular, strain-free olivine crystals (ol) growing on olivine porphyroclasts (ol-p) with closely spaced subgrain boundaries. (e) Partially recrystallized M1 harzburgite ET66 showing an orthopyroxene porphyroclast (opx-p) with embayments filled by tabular olivine crystals (ol), arrows indicate small interstitial orthopyroxene crystals within recrystallized domains. (f) Partially recrystallized M1 harzburgite ET84 displaying an irregularly shaped orthopyroxene porphyroclast (opx-p) with kinks (arrow) and exsolutions surrounded by olivine crystals (ol) with low densities of intracrystalline deformation features and polygonal grain boundaries. (g) Annealed coarse-porphyroclastic lherzolite ET53 showing irregularly shaped orthopyroxene crystals (opx) with cusp-like terminations. (h) Coarse-granular M1 lherzolite ET46 showing irregularly shaped orthopyroxene crystals (opx) with cusp-like terminations (marked by arrows) and olivine crystals (ol) with polygonal grain boundaries.

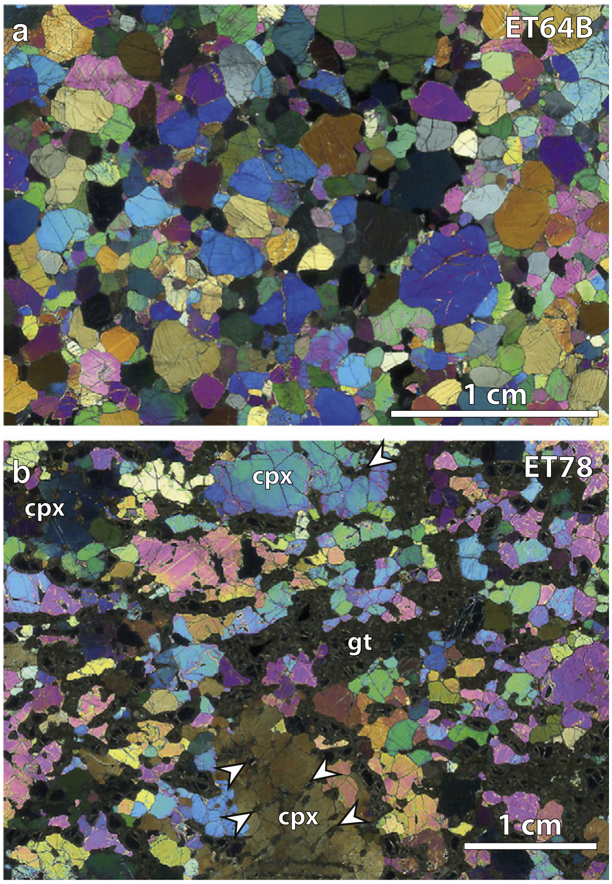

Fig. 7. Photomicrographs in plane-polarized light showing typical microstructures of Mega pyroxenites. (a) Coarse-granular spinel-websterite ET64. (b) Coarse-porphyroclastic garnet-clinopyroxenite ET78; note the undulose extinction and the kelyphitized garnet inclusions (arrows) in clinopyroxenite porphyroclasts (cpx) as well as larger kelyphitized garnet (gt) aggregates.

4.3. Crystallographic preferred orientations

Olivine, orthopyroxene, and clinopyroxene CPOs of all peridotites are presented in Fig. 8. Olivine CPOs have moderate to weak intensities and dominantly orthorhombic patterns, characterized by mutually orthogonal point maxima of [100], [010], and [001], with [100] and [010] usually displaying stronger concentrations than [001]. Some samples (ET35, ET54, ET48, ET70, ET76) have olivine CPO intermediate between orthorhombic and fiber-[100], characterized by a point maximum of [100] and a tendency of both [010] and [001] to form a girdle normal to it. Orthorhombic patterns with a tendency toward a fiber-[010] symmetry are also observed (ET38, ET71, ET73, ET82). In most samples, the relation between the CPO and a shape-preferred orientation (SPO) cannot be analyzed, because a SPO cannot be identified. However, in partially recrystallized samples ET66, ET84 and ETVB1, the concentration of [100] is subparallel to the elongation of the tabular recrystallized crystals (and of the porphyroclasts in ETVB1) and the [010] maximum subparallel to their short axis. These observations, together with stronger concentrations of [100] and [010] relative to [001], and with the predominance of <0vw> rotation axes in the accommodation of the intragranular misorientations, point to dominant activation of the [100](010) system in olivine. The olivine CPO data are summarized in Fig. 9, which presents the strength of the olivine CPO (characterized by the J-index) versus its symmetry (characterized by the BA-index). J- and BA-index data for all samples are also shown in Table 1. There is no correlation between the olivine CPO strength and symmetry. There is also no systematic variation of the olivine CPO symmetry or strength as a function of the type of metasomatism that affected the peridotites.

Orthopyroxene CPOs are much more variable than the olivine ones (Fig. 8). 4/9 of the M1 peridotites (ET35, ET69, ET83, ET84), 4/10 of the M2 peridotites (ET48, ET70, ET76, ET80), and 5/10 of the peridotites for which there is no REE data (ETVB1, ET30, ET73, ET82, ET85) display orthopyroxene CPO characterized by [001] and [100] maxima subparallel to the olivine [100] and [010] maxima, respectively. This is consistent with coherent deformation of both minerals, the orthopyroxene deforming dominantly by [001](100) glide. However, at least half of samples in each group show orthopyroxene CPOs that are not consistent with the olivine ones. These CPO are either very weak or are characterized by a maximum of [001] at high angle (45–90°) to the olivine [100] maximum (Fig. 8).

The clinopyroxene CPO exhibits an even greater lack of consistency with the olivine CPO than the orthopyroxene CPO (Fig. 8). Most peridotites that show coherent olivine and orthopyroxene CPOs have clinopyroxene CPO characterized by concentrations of [001] and of [100]* (the normal to the (100) plane) subparallel to the orthopyroxene [001] and [100] maxima, respectively. However, some (ET35, ET48, ET76, ET80, ET71, and ET73) display clinopyroxene CPO uncorrelated to the olivine and orthopyroxene CPOs. In peridotites in which olivine and orthopyroxene CPOs are inconsistent, the clinopyroxene CPO is often consistent with the orthopyroxene CPO, but more dispersed (Fig. 8). An exception is ET66, which has an olivine CPO uncorrelated with the orthopyroxene CPO, but correlated with the clinopyroxene one (Fig. 8).

In most pyroxenites, coarse grain sizes and exsolution textures hindered the acquisition of representative CPO. When enough grains were analyzed, orthopyroxene and clinopyroxene CPO have weak orthorhombic patterns. ET77 and ET81 have coherent orthopyroxene and clinopyroxene CPOs. In ET55 and ET64, they are not correlated.

4.4. Seismic properties

The similarity in olivine CPO symmetry (predominance of orthorhombic patterns) results in similar seismic anisotropy patterns for all Mega peridotites. The individual seismic anisotropy patterns are therefore presented as Supplementary Material (Fig. S1). Seismic anisotropy intensities for individual samples are nevertheless variable (Table 3). In the peridotites, the maximum P-wave propagation anisotropy is comprised between 2.4 and 12.3%, maximum S-wave polarization anisotropy ranges between 1.9 and 8.3% (Fig. 10), and maximum propagation anisotropies for fast (S1) and slow (S2) waves range between 1.2 and 5.8% and 1 and 6.1%, respectively. The maximum intensity of seismic anisotropy for both P- and S-waves show a gross positive correlation with olivine CPO intensity and modal content and a negative correlation with the clinopyroxene modal content (Fig. 10a,c,d), but no systematic variation function of the olivine CPO symmetry (Fig. 10b) The dispersion in Fig. 10a and c results from uncorrelated variations in olivine modal content and CPO intensity.

In Fig. 11, we present average seismic anisotropy patterns calculated based on the elastic constants of all peridotites and of the 6 pyroxenites for which representative CPO were obtained. Although many peridotites do not show a clear shape preferred orientation defining the foliation and lineation, based on the analysis of the CPOs and of the misorientation data, we concluded that in the present xenolith suite the olivine [100] maximum is parallel to the lineation and the [010] one, normal to the foliation. We then calculated average seismic properties supposing a common orientation of the foliation and lineation, that is, a coherent deformation of the entire lithospheric mantle beneath Mega. In the average peridotite, the P-wave propagation is the fastest close to the lineation and the slowest, normal to the foliation. S-wave polarization anisotropy is the highest for waves propagating parallel to the foliation plane and normal to the lineation, and the lowest for directions within 30° of the lineation in the XZ plane. For all propagation

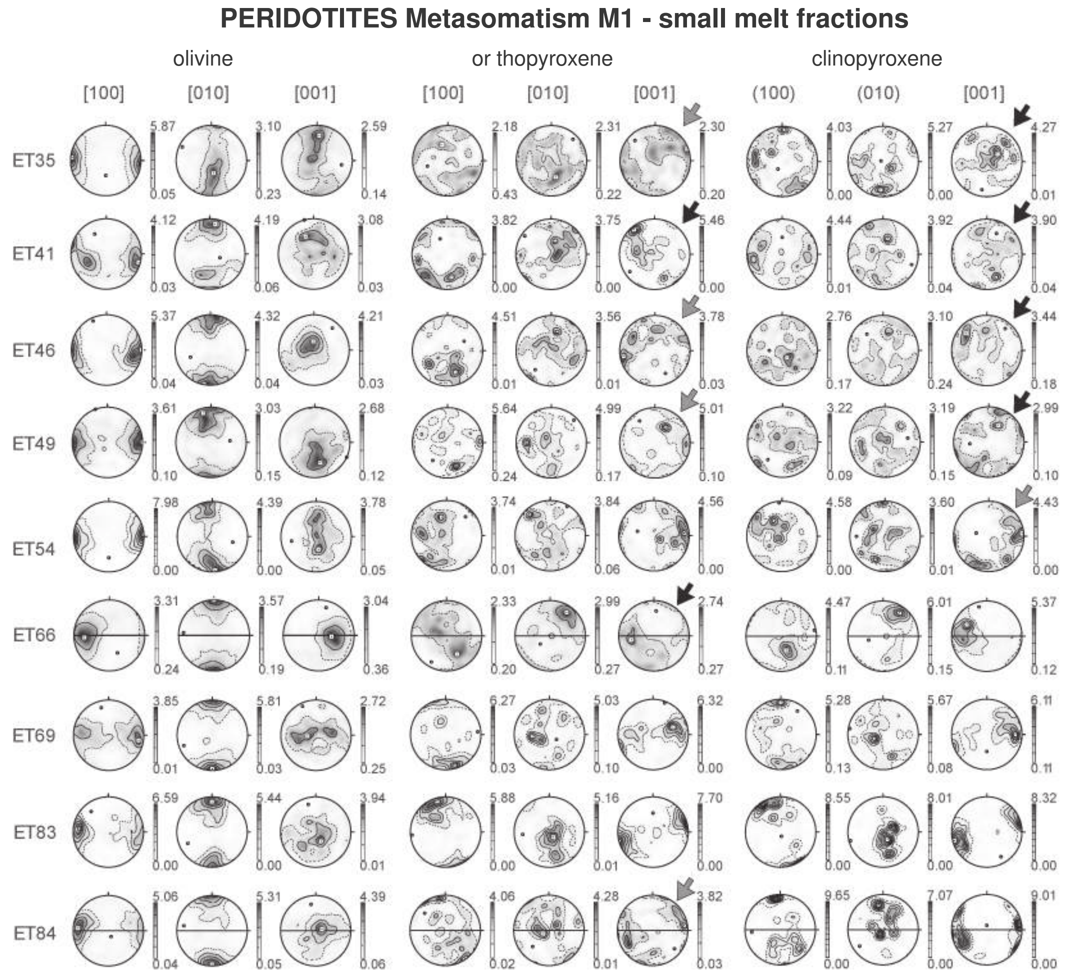

Fig. 8. Olivine, orthopyroxene, and clinopyroxene crystal preferred orientations of all studied peridotites. Lower hemisphere stereographic projections, contours at 1 multiples of a uniform distribution intervals. Maximum and minimum concentrations are indicated on the scale bar at the right of each pole figure. Black arrows mark pyroxene CPO uncorrelated with the olivine CPO, gray arrows, partially correlated ones. Full line marks the foliation (olivine shape preferred orientation), when visible in the thin section.

directions, the fast split S-wave is polarized parallel to the lineation. S1 waves propagate faster within the foliation plane, with the highest velocities at ca. 45° to the lineation, and slower normal to the foliation. S2 waves have slow velocities for all propagation directions at high angle to the lineation and are the fastest within 30° of the lineation in the XZ plane. The highest Vp/Vs_1 ratio is detected for waves propagating parallel to the lineation and the lowest Vp/Vs_1, for waves propagating normal to the foliation.

The average pyroxenite has a much weaker anisotropy and more complex patterns. Yet, comparison between the seismic properties of the average peridotite and of the average peridotites + pyroxenites sample indicates that the sole effect of increasing the proportion of pyroxenites up to 13% in the lithospheric mantle beneath Mega is to slightly decrease the seismic anisotropy.

Fig. 12 shows the intensity of azimuthal anisotropy that would be detected by horizontally propagating Pn, Love and Rayleigh waves, the birefringence of vertically propagating SKS waves, and the polarization anisotropy of surface waves (ε) calculated considering the average seismic properties of Mega xenoliths for different end-member orientations of the foliation and lineation in the lithospheric mantle. In all cases where the lineation is horizontal, horizontally polarized S-waves are faster than vertically polarized ones ($\varepsilon > 1$). A horizontal foliation results in moderate azimuthal anisotropy for Pn and Rayleigh waves (3.4 and 2%, respectively), moderate SKS splitting (2%), and extremely low Love wave azimuthal anisotropy (0.5%). A horizontal lineation in a moderate to strongly dipping foliation produces strong Pn azimuthal anisotropy (5.1%). SKS splitting is maximum (3.3%) for vertical foliations and decreases with the decrease in the dip of the foliation plane (2.4% for a 45° dip). Rayleigh wave azimuthal anisotropy also decreases slightly with the decrease in the dip of the foliation plane (2.4% for a vertical foliation and 2% for a 45°-dipping foliation). Love waves azimuthal anisotropy is always low, but slightly higher for 45°-dipping foliation (1.7%). A vertical lineation results in low anisotropy for all wave types (1.7% for Pn waves and 1.3% of SKS splitting and surface waves azimuthal anisotropy) and in faster propagation of vertically polarized surface waves ($\varepsilon < 1$). A 45°-dipping foliation with a downdip lineation produces the highest Rayleigh and Love waves azimuthal anisotropy (3.8% and 2.4%, respectively), but moderate SKS splitting (2.9%) and Pn azimuthal anisotropy (3.2%). Moreover, this orientation of the foliation and lineation results in inversion between the fast and the slow surface wave (Love or Rayleigh) as a function of the propagation direction (back-azimuth).

5. Discussion

Based on their equilibration temperatures (and pressure for the garnet pyroxenite), the peridotites and pyroxenites xenoliths from Mega sample a hot and thin lithospheric mantle between 35 and 60 km. This is consistent with estimates of the depth of the lithosphere-asthenosphere boundary at <80 km from surface wave data (Pasyanos and Nyblade, 2007; Fishwick, 2010). The analysis of the xenoliths' microstructure highlights a complex evolution of the lithospheric mantle

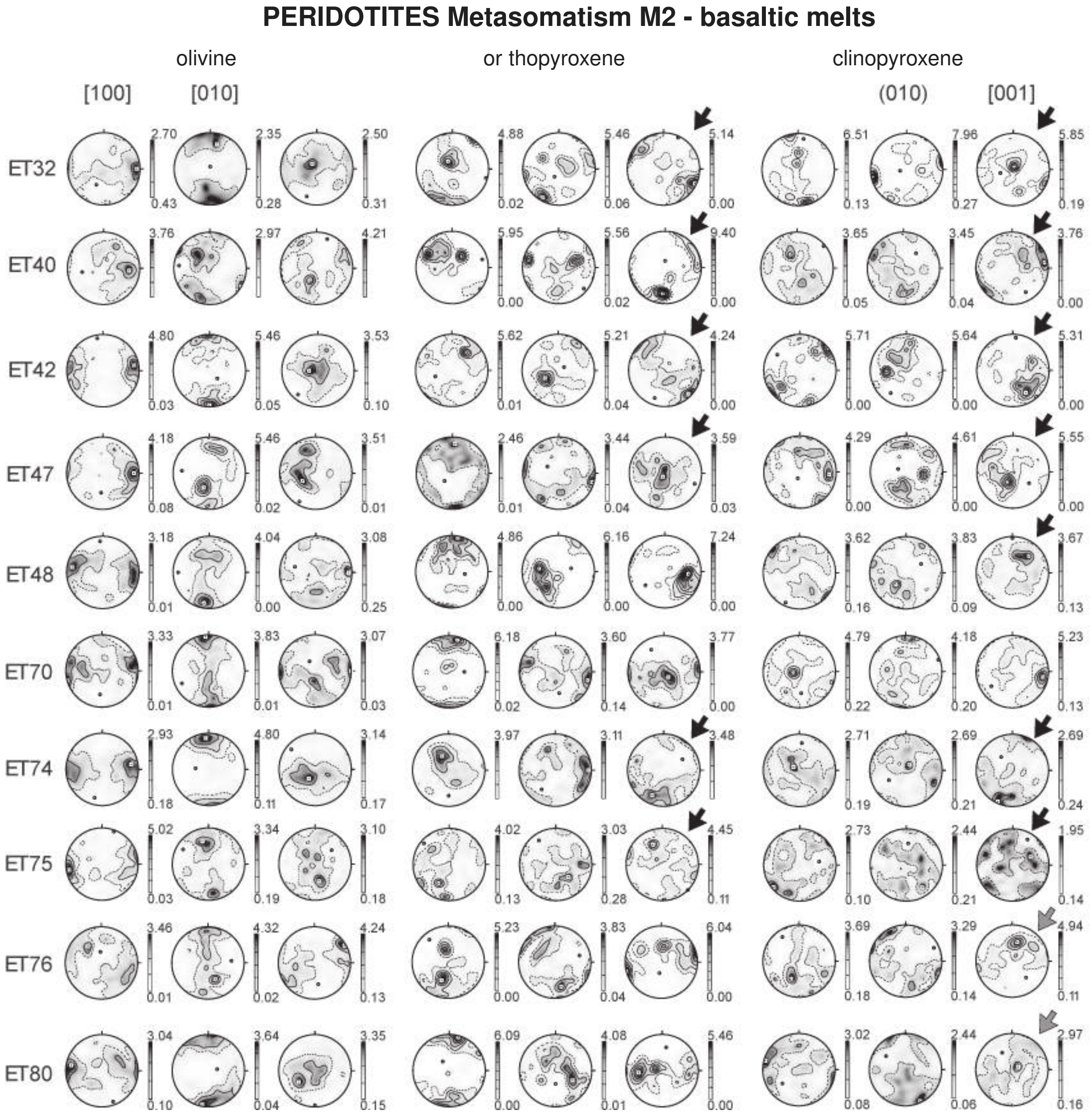

Fig. 8 (*continued*).

in the flanks of the southern Ethiopian rift, characterized by a pervasive low-stress deformation (which may be rift-related or older) followed by spatially variable degrees of static recrystallization. Microstructural observations also provide evidence for multiple events of reactional melt percolation, which led to extensive, but spatially heterogeneous refertilization of the lithospheric mantle. The two metasomatism types may be explained by spatially heterogeneous melt percolation. They may record an evolution in the composition of the melt in a vertical percolation column, the deeper parts of the column acquiring M2 compositions and the shallower ones, M1 compositions. However, if melt transport is focused, the two metasomatism types may also record the difference between the main conduit, where interactions with large volumes of melt produce M2 compositions, and a reactional domain in the wall-rock, where M1 compositions are formed by reaction with low melt fractions. Microstructural observations support that at least part of the refertilization postponed deformation, suggesting that reactive melt infiltration into the lithospheric mantle off the rift-axis was not systematically accompanied by widening of the domain accommodating the rifting deformation. It is important to stress that the present observations do not corroborate the previous interpretation by Bedini et al. (1997), which linked the different geochemical signatures of the metasomatism, namely the interaction with small melt fractions (M1) and with larger volumes of basaltic melts (M2), to systematic changes in the microstructure. Reactive melt percolation probably favored annealing, but there is no one-to-one relation between the intensity of melt-rock interactions and annealing. In this section, we summarize the microstructural and petrological evidence corroborating these conclusions (a sketch summarizing the inferred evolution is presented in Fig. 13) and compare the present observations to data from other xenolith localities and seismic observations in the East African rift system.

5.1. Relations between deformation, static recrystallization, and metasomatism

Peridotite xenoliths from Mega exhibit dominantly coarse-porphyroclastic microstructures (Fig. 4), characteristic of deformation by dislocation creep under low stress, probably high temperature conditions. Analysis of the olivine CPO and low-angle misorientation data, which imply dominant activation of [100]{0kl} systems, corroborates this interpretation. The variations in subgrain boundary spacing, in average intragranular misorientation, and in sinuosity of grain boundaries among the peridotites (Figs. 4, 5 and 6) indicate nevertheless that this deformation was followed by variable degrees of annealing (static recovery and recrystallization). Annealing may also explain why medium and coarse granular peridotites with 'undeformed' microstructures

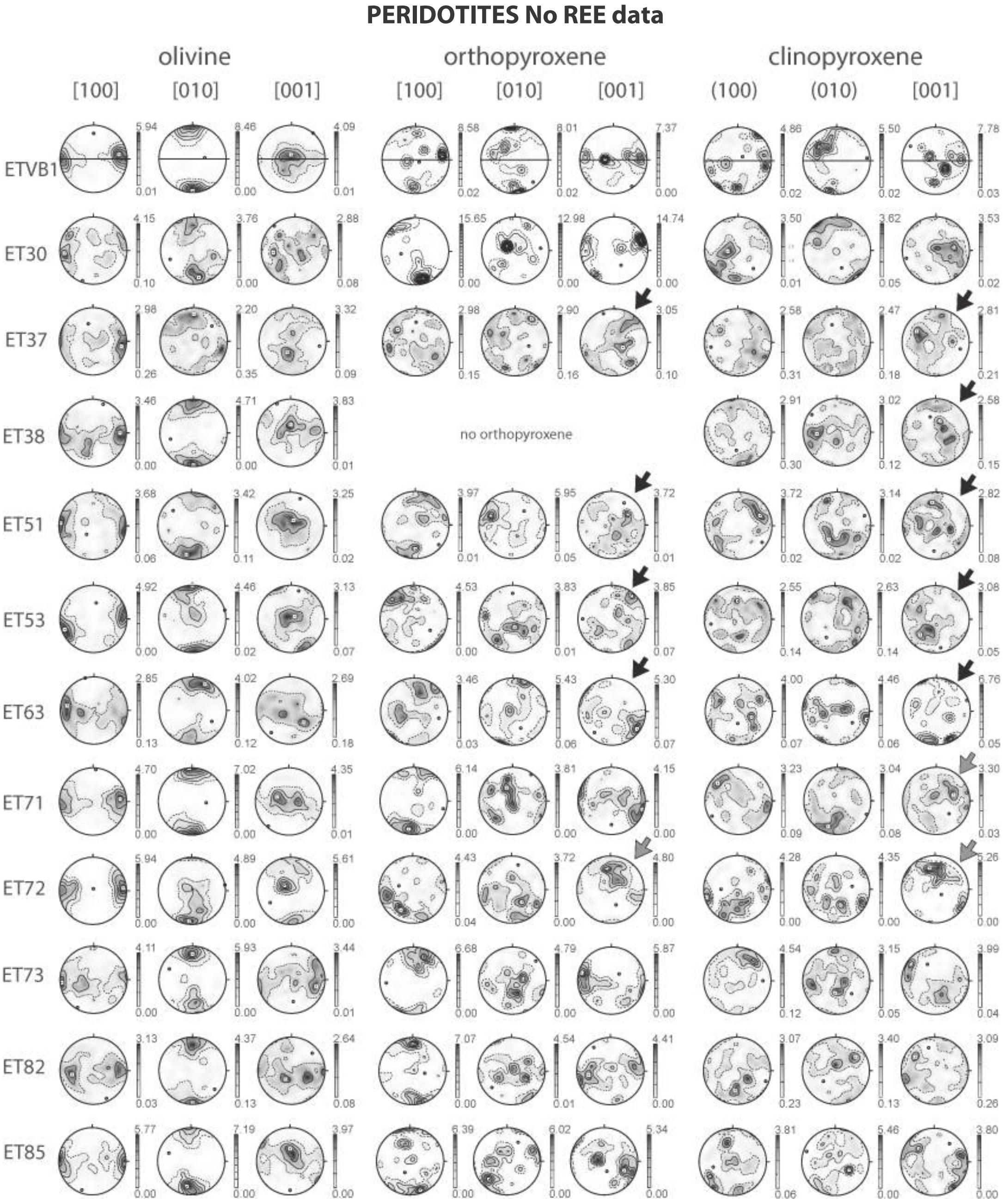

Fig. 8 (*continued*).

(absence of a SPO and low density of intragranular deformation features, quantified by low average M2M values <2.5°, cf. Figs. 4, 5 and 6), show clear olivine CPO (Fig. 8).

The partially recrystallized microstructures, characterized by growth of strain-free polygonal neoblasts over relict porphyroclasts with closely spaced subgrain boundaries, are a particular feature of the Mega xenolith suite. Coherence between the shape of the olivine neoblasts in ET66 and ET84 (Fig. 6d, e, f) and their CPO (the long axis of the crystals is parallel to the [100] maximum concentration and the short one, to the [010] maximum) suggests a crystallographic control on the growth of the neoblasts. The analysis of the microstructure does not permit to determine unambiguously whether the recrystallization is static or dynamic. Based on the coarse grain sizes, the very low internal misorientations, and the polygonal shapes of the recrystallized olivines, we favor nevertheless the hypothesis of a static recrystallization.

Mantle xenoliths from Mega also exhibit compositional, microstructural, and geochemical evidence for variable degrees of interaction with melts of basaltic or more evolved compositions. Variation in the melt–rock reaction products, sometimes within a sample, points to changes in the melt composition and implies multiple events of reactive melt percolation. Refertilization, that is, reactive melt percolation leading to crystallization of pyroxenes at the expense of olivine, predominates (Fig. 2), but early reactive melt percolation leading to crystallization of olivine at the expenses of pyroxenes (dunitization) is recorded by the absence of orthopyroxenes in wehrlite ET38 and by the presence of embayments filled by olivine in coarse orthopyroxenes in recrystallized peridotites ET66 and ET74 (Fig. 6e).

The present microstructural data does not allow fully constraining the relative timing between deformation, annealing, and metasomatic events. Pre- or synkinematic melt percolation may have occurred, but evidence for these early melt percolation episodes in the

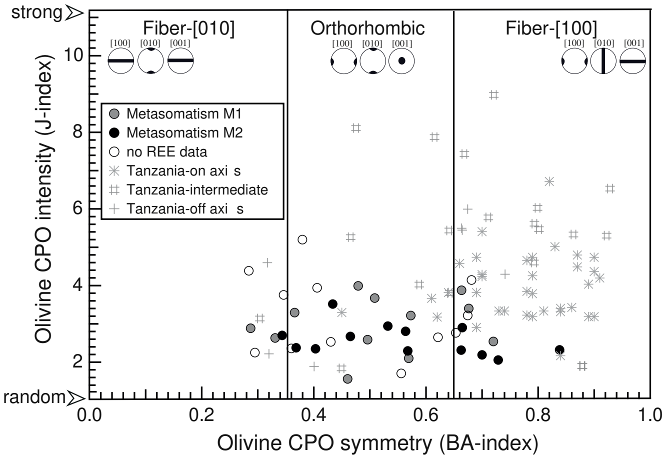

Fig. 9. Olivine CPO intensity (J-index) vs. symmetry (BA-index) for all samples as a function of the metasomatism type. Olivine CPO data for peridotite xenoliths from the Tanzanian Divergence (Baptiste et al., 2015) is shown for comparison.

microstructural record is patchy. For instance, in wehrlite ET38, olivine shows extensive and well-developed intracrystalline deformation features, which indicate that the olivine-producing reactive melt percolation that consumed the orthopyroxene is pre- or syn-deformation. The coexistence of deformed and undeformed pyroxenites also corroborates spatial heterogeneity and multiple episodes of magmatic percolation and deformation. Indeed, the pyroxenites were interpreted by Bedini (1994) as magmatic cumulates formed during the same event that produced the M2 metasomatism in peridotites. Most exhibit magmatic or metamorphic (cooling) microstructures (Fig. 7a), but some show partially recrystallized microstructures (Fig. 7b), which suggest that, locally, significant deformation (finite strains high enough to produce recrystallization) postdated the reactive melt percolation.

Microstructural observations put stronger constraints on the latest events. In all studied peridotites, pyroxenes have very irregular shapes, with cusp-like terminations (Figs. 2, 4, and 6). Such features are unstable during deformation, suggesting that these crystals underwent at most incipient deformation after the last refertilization episode. Microstructural evidence supports therefore that the latest refertilization event postdated the main deformation episode. A later, very low strain, but high stress event recorded by the high density of subgrains and well developed undulose extinction in a few samples, like ET32 (Fig. 6a), might be related to diking and xenolith extraction processes (Goetze, 1975).

The lack of correlation between the olivine and pyroxenes CPOs in roughly half of the studied peridotites corroborates post-kinematic refertilization (addition of pyroxenes) by reactive melt percolation.

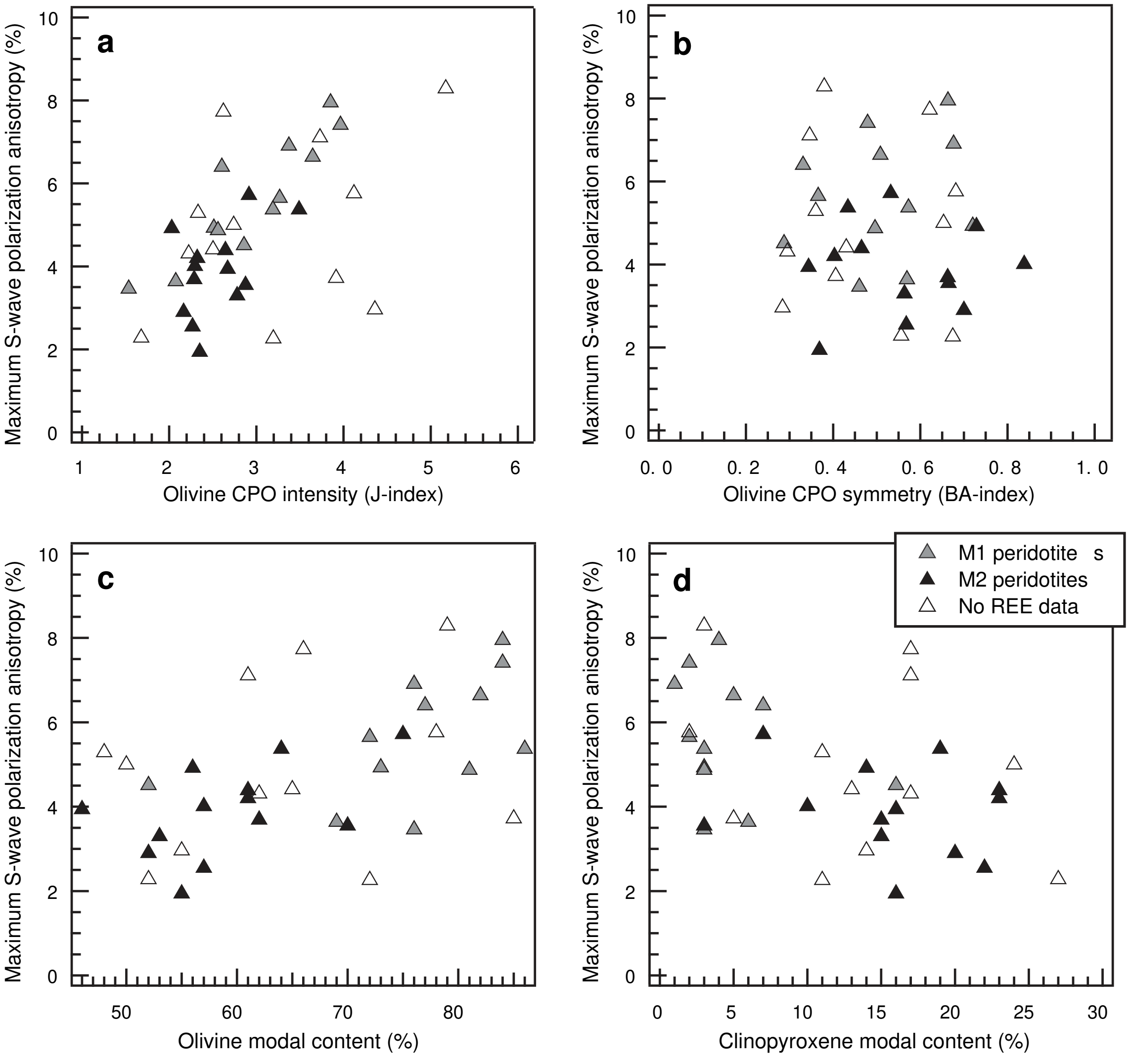

Fig. 10. S-wave polarization anisotropy of Mega peridotites vs. (a) olivine CPO intensity (J-index), (b) olivine CPO symmetry (BA-index), (c) olivine modal content, and (d) clinopyroxene modal content.

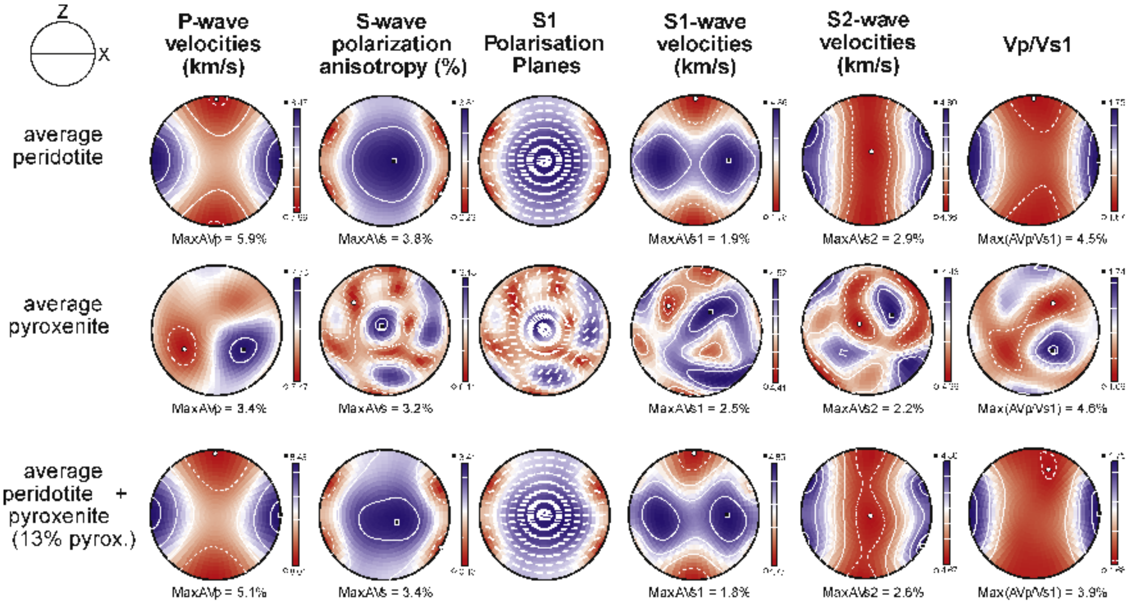

Fig. 11. Average seismic anisotropy patterns calculated based on the seismic constants for all peridotites (40 thin sections analyzed by EBSD, Table 1) and 5 pyroxenites (6 thin sections analyzed by EBSD; samples ET55, ET64, ET68, ET77, ET81 in Table 2). From left to right are displayed the 3-D distributions of P-wave velocities (Vp), S-wave polarization anisotropy (AVs) and the orientation of fast shear wave polarization plane, S1 wave velocities (VS1), S2 wave velocities (VS2), and the Vp/VS1 ratio. Lower hemisphere stereographic projections. Black squares and white circles indicate maximum and minimum values, respectively. Top left insert shows the structural reference frame.

However, many of the peridotites that exhibit clear compositional and microstructural evidence for refertilization show correlated olivine and pyroxenes CPO. Does this imply that reactive melt percolation locally predated deformation? As discussed above, the shapes of the pyroxenes indicate that any deformation that postdated the reactive melt percolation episodes producing refertilization resulted in very low finite strains. If refertilization occurred under static conditions, correlation between olivine and pyroxenes CPOs may be explained if the reactions resulted in further growth of pre-existing deformed pyroxene crystals rather than crystallizing new grains. In this case, the kinks in orthopyroxene porphyroclasts and the undulose extinction in both ortho- and clinopyroxenes might also be inherited from the main deformation episode or, as proposed before, record local deformation related to xenolith extraction processes.

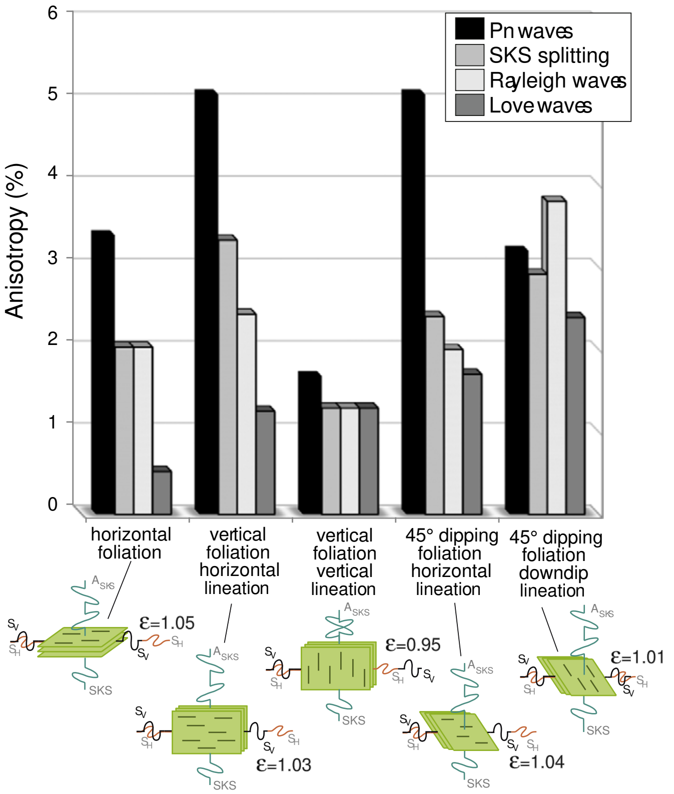

Fig. 12. Intensity of azimuthal anisotropy of horizontally propagating Pn, Love and Rayleigh waves, birefringence of vertically propagating SKS waves, and polarization anisotropy (ε) of surface waves calculated considering the average peridotites + pyroxenites seismic properties for different end-member orientations of the foliation and lineation in the lithospheric mantle beneath Mega. Data used for producing this figure is presented in Table 4.

Reactive melt percolation may have favored annealing. In most Mega peridotites, microstructural evidence of melt-rock reaction is homogeneously distributed within the samples, suggesting porous flow (Figs. 2, 4, and 6). The presence of intergranular melt films creates fast diffusion paths. It may therefore have favored the growth of polygonal neoblasts in the partially recrystallized peridotites and the almost complete reequilibration of grain shapes in some of the coarse-porphyroclastic samples, like ETVB1 (Fig. 4d). Grain growth favored by fluid films along grain boundaries has indeed been proposed by Drury and Van Roermund (1989) to explain development of euhedral olivine crystal in kimberlite-borne peridotite mylonites. Presence of intergranular melt films during annealing might also explain why in some samples grain boundary migration was favored relative to recovery, leading to inconsistency between grain boundary morphology and intragranular misorientation in the Mega peridotites. However, there is no simple relation between geochemical indicators of the intensity of the metasomatism, such as the perturbation of the modal compositions and the enrichment in trace elements, and microstructural evolution due to annealing (Fig. 5). There is also no correlation between equilibration temperatures and intensity of annealing (Table 1).

5.2. Comparison with data from other xenolith localities in the East African rift

Fig. 2a compares the compositions of Mega peridotites to those of mantle xenoliths from other localities in the East African rift system. Modal compositions of Mega peridotites are similar to those of xenoliths from the Marsabit volcanic field in the Turkana depression (Kaeser et al., 2006). Localities from the northern Ethiopian rift (Dedessa and Injibara), which are within the continental flood basalt extrusion domain, display a higher proportion of very fertile, pyroxene-rich lherzolites (Beccaluva et al., 2011). In contrast, localities from the Tanzanian divergence (Eledoi, Pello Hill, Olmani, and Lashaine), which sample a younger domain of the East African rift that has been affected by lower volumes of magmatism, show much more refractory compositions, which range from orthopyroxene-rich harzburgites to dunites (Baptiste et al., 2015 and references therein). A change in the dominant type of melt–rock reactions in the lithospheric mantle along the rift system is corroborated by microstructural observations, which indicate that crystallization of olivine at the expenses of pyroxene predominated in the Tanzanian peridotite xenoliths, whereas refertilization reactions prevailed in Mega and northern Ethiopian peridotites. This change probably records variations in the percolating magma composition due to differences in partial melting depths and degrees and in the melt transport processes (Fig. 14). High degrees of shallow melting in the mature northern East African rift produce tholeitic basalts. Reactive percolation of these melts will produce refertilization. This process is similar to the refertilization atop of a melting front described in the Lherz and Ronda peridotites massifs (Le Roux et al., 2007; Soustelle et al., 2009). On the other hand, deep low degrees of melting in the younger southern sections of the East African rift produce alkaline basalts. If these melts are transported at fast rates through the lithosphere, by channeling along shear zones, for instance, they will be in chemical disequilibrium and produce dunitization reactions in the lithospheric mantle (e.g., Kelemen and Dick, 1995).

Microstructures also differ among the various xenolith localities in the East African rift. Mega peridotites show mainly coarse-porphyroclastic microstructures, with variable degrees of annealing. Fine-grained porphyroclastic and mylonitic microstructures, which are observed in peridotite xenoliths from Marsabit (Kaeser et al., 2006; Kaczmarek and Reddy, 2013) and from on-axis volcanoes in the Tanzanian Divergence (Baptiste et al., 2015), are absent among Mega peridotites. One may question whether the partially recrystallized microstructures in the Mega suite represent annealed equivalents of those mylonites. However, the partially recrystallized peridotites from Mega lack highly elongated orthopyroxenes, which are characteristic of the high-stress deformation that formed the mylonites in Marsabit and Pelo Hill. Annealing cannot erase this grain elongation. Orthopyroxene shapes may be modified by melt-rock reactions, but analysis of the orthopyroxenes in the Mega recrystallized peridotites does not show any evidence (residual elongation or alignment of relict crystals with similar orientations) of initial aspect ratios >10:1. This suggests that, differently from the other two localities, intense high stress deformation, implying strain localization, did not occur in the lithospheric mantle beneath Mega.

The Mega peridotite suite also shows a smaller proportion of granular peridotites than the northern Ethiopian xenolith suites (Beccaluva et al., 2011) and than the off-rift axis Lashaine peridotites from the Tanzanian Divergence (Baptiste et al., 2015). The more pyroxene-rich compositions of the peridotites from the northern Ethiopian localities (Beccaluva et al., 2011), suggest that they sampled a mantle that has experienced percolation of large volumes of magma (integrated through time), consistently with their location within the continental flood basalt province. Interaction with larger volumes of magmas may have favored annealing of rift-related or older deformation structures in the lithospheric mantle beneath the Ethiopian plateau. The Lashaine peridotites, on the other hand, might represent an older lithospheric domain, which has not been reactivated by the rifting (Dawson, 2002; Baptiste et al., 2015).

Comparison of the olivine CPOs in the Mega peridotites with those from xenoliths from the Tanzanian Divergence reveals that Mega peridotites have weaker CPO with more orthorhombic patterns (Fig. 9). The contrast in olivine CPO symmetry and intensity is particularly marked when the comparison is made with peridotites from on-axis localities of the Tanzanian Divergence, which exhibit dominantly strong olivine CPOs with a fiber-[100] symmetry. Lower strain intensities or a more developed annealing in the lithospheric mantle beneath Mega may explain this change in olivine CPO pattern. Peridotites from Marsabit display dominantly weak to moderate olivine CPO with orthorhombic to fiber-[010] symmetries (Kaczmarek and Reddy, 2013), similar to Mega peridotites. No CPO data is available for xenoliths from northern Ethiopia.

In summary, analysis of a ~N–S xenolith-based profile along the East African rift system from northern Ethiopia to the Tanzanian Divergence highlights a decrease in the importance of magmatic processes in the lithospheric mantle, consistent with the decrease in the volume of magmatic products at the surface (Fig. 14). Xenoliths occasionally display evidence for localized deformation, expressed as mylonitic microstructures recording intense high-stress deformation that may be rift-related However, these features are only observed in the southern xenolith-bearing localities: Marsabit in the Turkana depression, where mylonites correspond to the least metasomatized samples (Kaeser et al., 2006), and on-axis sites in the Tanzanian Divergence (Baptiste et al., 2015). At first sight, these data suggest an anti-correlation between pervasive magma flux through the lithosphere, leading to refertilization, and localized, high stress deformation. The data is, however, too patchy for discriminating between a temporal evolution (localized, high stress deformation of an initially cold lithosphere) or a spatial variation in deformation style. Indeed, the Mega and Ethiopian plateau localities, which do not contain mylonites, are both offset from the rift axis.

5.3. Anisotropy in the lithospheric mantle beneath the southern Ethiopian rift

The average seismic properties of the Mega xenolith suite indicate that the lithospheric mantle beneath the southern part of the main Ethiopian rift has a low to moderate seismic anisotropy. This low anisotropy results from both the rather weak olivine CPO and the high proportion of pyroxenes that characterize this xenolith suite. As discussed in Section 2, the southern part of the Ethiopian rift is poorly covered by seismological data. We have to compare the seismic properties calculated from the xenolith data with seismic data obtained north and south of the study region. Estimates for crustal and lithospheric thickness beneath the Ethiopian rift from shear velocity models range between 25–35 km, and 70–80 km, respectively (Dugda et al., 2007). Based on these data, which suggest a 35–55 thick lithospheric mantle with S-wave velocities in the range 4.1–4.2 km/s (Dugda et al., 2007) and the average seismic properties of the Mega xenolith suite, we may estimate SKS delay times for different orientations of the foliation and lineation (Fig. 12). Maximum delay times, in the range of 0.28–0.45 s, are predicted for vertical foliations and horizontal lineations. Horizontal lineations are also required to explain the rather high P-wave velocities measured beneath the northern part of the rift-parallel KRISP refraction profile in Kenya (Mechie et al., 1994). Even in this most favorable case, the predicted delay times are much lower than those measured in the Afars and in the northern and central Ethiopian rift (0.5–3 s; Gashawbeza et al., 2004; Kendall et al., 2005). This comparison corroborates the interpretation that most of the anisotropic signal beneath the main Ethiopian rift and in the Afars results from oriented melt pockets, which may be located in the crust, lithospheric mantle, or asthenosphere (Kendall et al., 2005; Hammond et al., 2014; Hammond and Kendall, 2016).

The delay times predicted based on the average Mega seismic properties are also lower than those predicted for the upper layer in stations offset from the rift in the Ethiopian plateau and Yemen (0.7–0.95 s), which are characterized by fast SKS polarization parallel to the pre-existing (Precambrian) structures and faster seismic velocities in the mantle (Hammond et al., 2014). Calculated delay times based on the Mega xenoliths data are also lower than those observed in stations in the Kenya rift (0.8–2.4 s; Gao et al., 1997; Walker et al., 2004). These

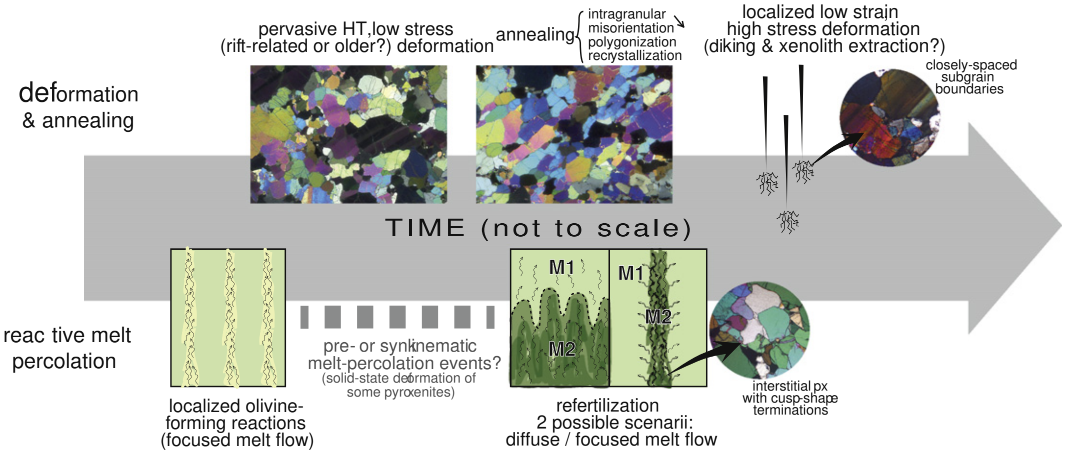

Fig. 13. Sketch summarizing the relative timing between deformation, annealing, and reactive melt percolation episodes inferred from the microstructural observations. Note that the time arrow has no scale, since there are no constraints on the absolute timing, duration, or time intervals between various processes.

observations suggest that the low intrinsic anisotropy observed beneath Mega is not a general feature of the Precambrian domains that surround the rift, but it is a consequence of the extensive reactive melt percolation recorded by the studied xenoliths. It might therefore be representative of the contribution of olivine crystal preferred orientations in the lithospheric mantle beneath the regions submitted to extensive magmatic percolation, such as the Main Ethiopian rift.

6. Conclusion

Analysis of the microstructures and crystal preferred orientations, together with previous geochemical data on a suite of 42 mantle xenoliths (32 peridotites and 10 pyroxenites) from Mega shows that the lithospheric mantle beneath the eastern flank of the southernmost Ethiopian rift segment in the East African rift system records evidence for:

(1) Reactive percolation of melts, mainly by porous flow-type mechanisms, but with volumes and compositions of the melts varying in space and, probably, also through time. This process resulted in a high variability in compositions, which range from LILE-enriched harzburgites (M1 metasomatism) to pyroxene-rich lherzolites depleted or only slightly enriched in LILE (M2 metasomatism), as well as olivine-websterites and pyroxenites.

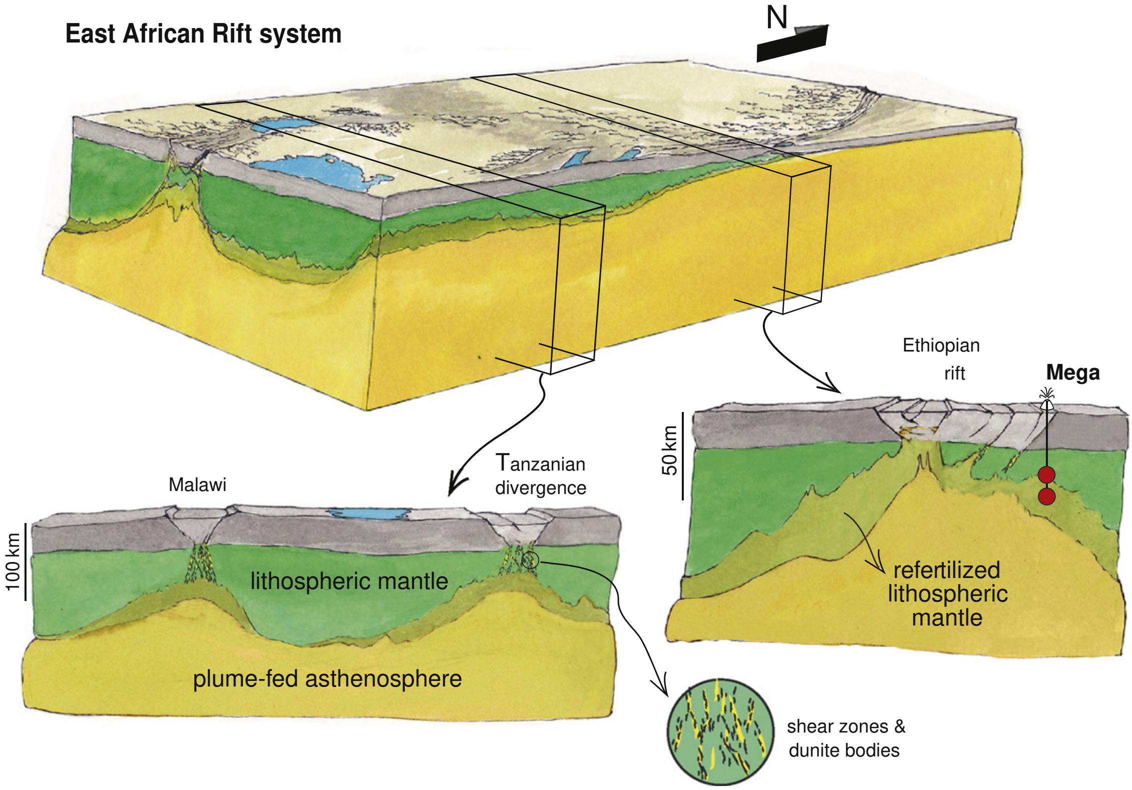

Fig. 14. Sketch of the East African Rift System illustrating the concept of change in space and time, function of the rift maturity and of the depth of the lithosphere-asthenosphere boundary, of the type of metasomatism of the lithospheric mantle due to reactive melt transport. Refertilization is favored in the vicinity of the melting domains, that is, at the base of the lithosphere, whereas dunitization reactions require chemical disequilibrium between the melts and the peridotites and are favored by fast melt transport (probably in shear zones) to shallow depths in the lithospheric mantle.

(2) Low-stress deformation by dislocation creep, which produced the coarse-porphyroclastic microstructures and orthorhombic [100](010) type olivine CPO. This deformation was followed by variable degrees of annealing, expressed as either recovery or grain boundary migration, and, locally by a recrystallization episode. The processes leading to recrystallization could not be unambiguously identified. However, based on the absence of stretched orthopyroxenes, which are typical features of high-stress deformation of peridotites, and the presence of embayments in coarse orthopyroxenes filled by deformation-free polygonal olivine crystals, we favor static recrystallization (and/or crystallization) of olivine favored by melt percolation.

The microstructural and CPO data also indicate that at least the last reactive melt percolation event, which resulted in refertilization and that is best expressed in the M2 lherzolites, postdates the main deformation. Static recrystallization in presence of melt may explain the equilibrated polygonal grain boundaries in some annealed samples and in the recrystallized ones. However, in contrast to previous conclusions by Bedini et al. (1997), we do not observe evidence for a simple relation between the intensity of annealing and the type and intensity of the metasomatism or the equilibration temperatures.

Another characteristic feature of Mega peridotites is their weak to moderate olivine CPO, which, together with enrichment in pyroxenes in many samples, result in a weak intrinsic seismic anisotropy of the lithospheric mantle beneath the eastern flank of the southernmost Ethiopian rift. Maximum anisotropies for all seismic wave types would be sampled if the lithospheric mantle beneath Mega had a vertical foliation (normal to the olivine $[010]_{max}$) and a horizontal lineation (olivine $[100]_{max}$): $AV_{P}max = 5.1\%$, $AV_{S}max = 3.4\%$, $AV_{Rayleigh}max = 2.6\%$. Even in this case, SKS delay times associated with solid-state deformation fabrics in the lithospheric mantle (i.e., in the absence of oriented melt pockets) would be <0.5 s. Comparison with seismic anisotropy data in other domains of the East African rift system submitted to less extensive melt percolation (that is, offset from the main magmatic centers) suggest, however, that this low anisotropy is a local feature, probably related to the extensive reactive melt percolation recorded by the studied xenoliths. Yet, the processes leading to the dispersion of the olivine CPO during reactive melt percolation, in particular when it results in refertilization, are still not understood. Another open question is whether this decrease in anisotropy is a general feature of lithospheric mantle domains submitted to extensive melt percolation under static conditions.

Finally, comparison with peridotite xenoliths from other localities within the East African rift system highlights a change in the dominant type of melt-rock reactions in the lithospheric mantle, which records variations in the percolating magma composition due to differences in partial melting depths and melt transport processes. Dunitization prevails in peridotites from the Tanzanian divergence, where deep melting beneath a thick lithosphere and, probably, melt channeling along shear zones produce magmas in strong disequilibrium with shallow lithospheric peridotites. In contrast, predominance of refertilization in Mega and in other localities from the Ethiopian and Kenyan rifts implies that the magmas that percolate the lithospheric mantle in these more mature domains were produced at shallower depths, consistently with geophysical data that suggest a thin lithosphere.

Acknowledgments

We thank J.L. Bodinier for numerous discussions on reactive melt percolation in the lithospheric mantle and Y. Takei and J. Hammond for their constructive reviews. D. Mainprice provided the softwares for analyzing the EBSD data and calculating seismic properties. C. Nevado and D. Delmas prepared high-quality polished thin sections for EBSD measurements. EBSD analyses were performed with the help of F. Barou at the EBSD–SEM national facility at Geosciences Montpellier. Giovanna Sapienza (formerly at Univ. Bologna) enabled us to retrieve the Mega xenoliths from Prof. Lauro Morten's collection. V.B. Ph.D. thesis was funded by the Ministère de la Recherche, France.

References

Abramson, E.H., Brown, M., Slutsky, L.J., Zaug, J., 1997. The elastic constants of San Carlos olivine up to 17 GPa. J. Geophys. Res. 102, 12,252–212,263.

Achauer, U., KRISP Teleseismic Working Group, 1994. New ideas on the Kenya rift based on the inversion of the combined dataset of the 1985 and 1989/90 seismic tomography experiment. Tectonophysics 236, 305–329.

Bachmann, F., Hielcher, R., Schaeben, H., 2011. Grain detection from 2d and 3d EBSD data — specification of the MTEX algorithm. Ultramicroscopy 11, 1720–1733.

Bachmann, F., Hielscher, R., Schaeben, H., 2010. Texture analysis with MTEX — free and open source software toolbox. Solid State Phenom. 160, 63–68.

Bagley, B., Nyblade, A.A., 2013. Seismic anisotropy in eastern Africa, mantle flow, and the African superplume. Geophys. Res. Lett. 40, 1500–1505.

Baptiste, V., Vauchez, A., Tommasi, A., Demouchy, S., Rudnick, R., 2015. Deformation, hydration, and anisotropy of the lithospheric mantle beneath an active rift: constraints from mantle xenoliths from the North Tanzanian Divergence. Tectonophysics 639, 34–55. http://dx.doi.org/10.1016/j.tecto.2014.1011.1011.

Barruol, G., Kern, H., 1996. Seismic anisotropy and shear-wave splitting in lower-crustal and upper-mantle rocks from the Ivrea zone — experimental and calculated data. Phys. Earth Planet. Inter. 95, 175–194.

Bastow, I., Nyblade, A., Stuart, G., Rooney, T., Benoit, M., 2008. Upper mantle seismic structure beneath the Ethiopian hot spot: rifting at the edge of the African low-velocity anomaly. Geochem. Geophys. Geosyst. 9, Q12022. http://dx.doi.org/10.1029/2008GC002107.

Bastow, I., Pilidou, S., Kendall, J.M., Stuart, G., 2010. Melt-induced seismic anisotropy and magma assisted rifting in Ethiopia: evidence from surface waves. Geochem. Geophys. Geosyst. 11, Q0AB05. http://dx.doi.org/10.1029/2010GC003036.

Beccaluva, L., Bianchini, G., Ellam, R.M., Natali, C., Santato, A., Siena, F., Stuart, F.M., 2011. Peridotite xenoliths from Ethiopia: inferences about mantle processes from plume to rift settings. In: Beccaluva, L., Bianchini, G., Wilson, M. (Eds.), Volcanism and Evolution of the African Lithosphere. Geological Society of America Special Paper, Washington, DC, pp. 77–104.

Bedini, R.-M., 1994. Studio Geochimico–Petrologico Degli Xenoliti Ultrafemici di Mega (Sidamo, Ethiopia — Rift Africano Orientale): Implicazione Sui Processi di Interazione Magma-Roccia Nel Mantello Litosferico Subcontinentale. Universita di Bologna, p. 253.

Bedini, R.M., Bodinier, J.-L., 1999. Distribution of incompatible trace elements between the constituents of spinel peridotite xenoliths: ICP-MS data from the East African Rift. Geochim. Cosmochim. Acta 63, 3883–3900.

Bedini, R.M., Bodinier, J.-L., Dautria, J.-M., Morten, L., 1997. Evolution of LILE-enriched small melt fractions in the lithospheric mantle: a case study from the East African Rift. Earth Planet. Sci. Lett. 153, 67–83.

Benoit, M.H., Nyblade, A.A., Pasyanos, M.E., 2006. Crustal thinning between the Ethiopian and East African plateaus from modeling Rayleigh wave dispersion. Geophys. Res. Lett. 33, L13301. http://dx.doi.org/10.11029/12006GL025687.

Bialas, R.W., Buck, W.R., Qin, R., 2010. How much magma is required to rift a continent? Earth Planet. Sci. Lett. 292, 68–78.

Boioli, F., Tommasi, A., Cordier, P., Demouchy, S., Mussi, A., 2015. Low steady state stresses in the cold lithospheric mantle inferred from dislocation dynamics models of dislocation creep in olivine. Earth Planet. Sci. Lett. 432, 232–242.

Bosworth, W., 1992. Mesozoic and tertiary rifting in East Africa. Tectonophysics 209, 115–137.

Brey, G.P., Köhler, T., 1990. Geothermobarometry in four-phase lherzolites II. New thermobarometers and practical assessment of existing thermobarometers. J. Petrol. 31, 1353–1378.

Buck, W.R., 2006. The role of magma in the development of the Afro-Arabian Rift System. Geol. Soc. Lond., Spec. Publ. 259, 43–54.

Bunge, H.J., 1982. Texture Analysis in Materials Sciences. Buttleworth, London.

Chai, M., Brown, J.M., Slutsky, L.J., 1997a. The elastic constants of a pyrope-grossular-almandine garnet up to 20 GPa. Geophys. Res. Lett. 24, 523–526.

Chai, M., Brown, J.M., Slutsky, L.J., 1997b. The elastic constants of an aluminous orthopyroxene to 12.5 GPa. J. Geophys. Res. 102, 14779–14786. http://dx.doi.org/10.11029/14797JB00893.

Chorowicz, J., 2005. The East African rift system. J. Afr. Earth Sci. 43, 379–410.

Civiero, C., Hammond, J.O., Goes, S., Fishwick, S., Ahmed, A., Ayele, A., Leroy, S., 2015. Multiple mantle upwellings in the transition zone beneath the northern East-African Rift system from relative P-wave travel-time tomography. Geochem. Geophys. Geosyst. 16, 2949–2968.

Collins, M.D., Brown, J.M., 1998. Elasticity of an upper mantle clinopyroxene. Phys. Chem. Miner. 26, 7–13.

Cornwell, D.G., Maguire, P.K.H., England, R.W., Stuart, G.W., 2010. Imaging detailed crustal structure and magmatic intrusion across the Ethiopian Rift using a dense linear broadband array. Geochem. Geophys. Geosyst. 11, Q0AB03.

Dawson, J.B., 2002. Metasomatism and partial melting in the upper-mantle peridotite xenoliths from the Lashaine Volcano, northern Tanzania. J. Petrol. 43, 1749–1777.

Djikstra, A.H., Drury, M.R., Vissers, R.L.M., Newman, J., 2002. On the role of melt–rock reaction in mantle shear zone formation in the Othris peridotite massif (Greece). J. Struct. Geol. 24, 1431–1450.

Drury, M.R., Van Roermund, H.L.M., 1989. Fluid assisted recrystallization in upper mantle peridotite xenoliths from kimberlites. J. Petrol. 30, 133–152.

Dugda, M.T., Nyblade, A.A., Julia, J., 2007. Thin lithosphere beneath the Ethiopian Plateau revealed by a joint inversion of Rayleigh wave group velocities and receiver functions. J. Geophys. Res. Solid Earth 112, B08305. http://dx.doi.org/10.01029/02006JB004918.

Ebinger, C., 2012. Evolution of the Cenozoic East African rift system: cratons, plumes, and continental breakup. Regional Geology and Tectonics: Phanerozoic Rift Systems and Sedimentary Basins: Phanerozoic Rift Systems and Sedimentary Basins, p. 133.

Ebinger, C., Bechtel, T., Forsyth, D., Bowin, C., 1989. Effective elastic plate thickness beneath the East African and Afar plateaus and dynamic compensation of the uplifts. J. Geophys. Res. 94, 2883–2901.

Ebinger, C.J., Yemane, T., Harding, D.J., Tesfaye, S., Kelley, S., Rex, D.C., 2000. Rift deflection, migration, and propagation: linkage of the Ethiopian and Eastern rifts, Africa. Geol. Soc. Am. Bull. 112, 163–176.

Ebinger, C.J., Yemane, T., Woldegabriel, G., Aronson, J.L., Walter, R.C., 1993. Late Eocene-recent volcanism and faulting in the southern main Ethiopian Rift. J. Geol. Soc. Lond. 150, 99–108.

Fishwick, S., 2010. Surface wave tomography: imaging of the lithosphere–asthenosphere boundary beneath central and southern Africa. Lithos 120, 63–73.

Furman, T., 2007. Geochemistry of East African rift basalts: an overview. J. Afr. Earth Sci. 48, 147–160.

Gao, S., Davis, P.M., Liu, H., Slack, P.D., Rigor, W., Zorin, Y.A., Mordvinova, V.V., Kozhevnikov, V.M., Logatchev, N.A., 1997. SKS splitting beneath continental rift zones. J. Geophys. Res. 102, 22781–22797.

Gashawbeza, E.M., Klemperer, S.L., Nyblade, A.A., Walker, K.T., Keranen, K.M., 2004. Shear-wave splitting in Ethiopia: Precambrian mantle anisotropy locally modified by Neogene rifting. Geophys. Res. Lett. 31, L18602. http://dx.doi.org/10.11029/12004GL020471.

Georges, R., Rogers, N., Kelley, S., 1998. Earliest magmastim in Ethiopia: evidence for two mantle plumes in one flood basalt province. Geology 26, 923–926.

Goetze, C., 1975. Sheared Iherzolites: from the point of view of rock mechanics. Geology 3, 172–173.

Hammond, J., Kendall, J.-M., 2016. Constraints on melt distribution from seismology: a case study in Ethiopia. Geol. Soc. Lond. Mem. 420. http://dx.doi.org/10.1144/SP420.14.

Hammond, J., Kendall, J.-M., Stuart, G.W., Ebinger, C.J., 2013. Mantle upwelling and initiation of rift segmentation beneath the Afar Depression. Geology 41, 635–638.

Hammond, J., Kendall, J.M., Wookey, J., Stuart, G., Keir, D., Ayele, A., 2014. Differentiating flow, melt, or fossil seismic anisotropy beneath Ethiopia. Geochem. Geophys. Geosyst. 15, 1878–1894.

Hansen, S.E., Nyblade, A.A., Benoit, M.H., 2012. Mantle structure beneath Africa and Arabia from adaptively parameterized P-wave tomography: implications for the origin of Cenozoic Afro-Arabian tectonism. Earth Planet. Sci. Lett. 319, 23–34.

Havlin, C., Parmentier, E., Hirth, G., 2013. Dike propagation driven by melt accumulation at the lithosphere–asthenosphere boundary. Earth Planet. Sci. Lett. 376, 20–28.

Hearmon, R.F.S., 1984. The elastic constants of crystals and other anisotropic materials. In: Hellwege, K.H., Hellwege, A.M. (Eds.), Landolt–Bornstein Tables. Springer-Verlag, Berlin, pp. 1–154.

Hielscher, R., Schaeben, H., 2008. A novel pole figure inversion method: specification of the MTEX algorithm. J. Appl. Crystallogr. 41, 1024–1037.

Hofmann, C., Courtillot, V., Feraud, G., Rochette, P., Yirgu, G., Ketefo, E., Pik, R., 1997. Timing of the Ethiopian flood basalt event and implications for plume birth and global change. Nature 389, 338–341.

Jakovlev, A., Rümpker, G., Schmeling, H., Koulakov, I., Lindenfeld, M., Wallner, H., 2013. Seismic images of magmatic rifting beneath the western branch of the East African Rift. Geochem. Geophys. Geosyst. 14, 4906–4920.

Kaczmarek, M.-A., Reddy, S.M., 2013. Mantle deformation during rifting: constraints from quantitative microstructural analysis of olivine from the East African Rift (Marsabit, Kenya). Tectonophysics 608, 1122–1137.

Kaeser, B., Kalt, A., Pettke, T., 2006. Evolution of the lithospheric mantle beneath the Marsabit volcanic field (northern Kenya): constraints from textural, P–T and geochemical studies on xenoliths. J. Petrol. 47, 2149–2184.

Kelemen, P.B., Dick, H.J., 1995. Focused melt flow and localized deformation in the upper mantle: juxtaposition of replacive dunite and ductile shear zones in the Josephine peridotite, SW Oregon. J. Geophys. Res. 100, 423–438.

Kendall, J.M., Stuart, G.W., Ebinger, C.J., Bastow, I.D., Keir, D., 2005. Magma-assisted rifting in Ethiopia. Nature 433, 146–149. http://dx.doi.org/10.1038/nature03161.

Kourim, F., Vauchez, A., Bodinier, J.-L., Alard, O., Bendaoud, A., 2015. Subcontinental lithosphere reactivation beneath the Hoggar swell (Algeria): localized deformation, melt channeling and heat advection. Tectonophysics 650, 18–33.

Le Roux, V., Bodinier, J.L., Tommasi, A., Alard, O., Dautria, J.M., Vauchez, A., Riches, A., 2007. The Lherz spinel-lherzolite: refertilized rather than pristine mantle. Earth Planet. Sci. Lett. 259, 599–612. http://dx.doi.org/10.1016/j.epsl.2007.1005.1026.

Lorand, J.P., Reisberg, L., Bedini, R.M., 2003. Platinum-group elements and melt percolation processes in Sidamo spinel peridotite xenoliths, Ethiopia, East African rift. Chem. Geol. 196, 57–75.

Mainprice, D., 1990. A FORTRAN program to calculate seismic anisotropy from the lattice preferred orientation of minerals. Comput. Geosci. 16, 385–393.

Mainprice, D., Bachmann, F., Hielscher, R., Schaeben, H., 2014. Descriptive tools for the analysis of texture projects with large datasets using MTEX: strength, symmetry and components. Geol. Soc. Lond., Spec. Publ. 409. http://dx.doi.org/10.1144/SP1409.1148.

Mechie, J., Fuchs, K., Altherr, R., 1994. The relationship between seismic velocity, mineral composition and temperature and pressure in the upper mantle—with an application to the Kenya Rift and its eastern flank. Tectonophysics 236, 453–464.

Morten, L., De Francesco, A.M., Bonavia, F., Haileselassie, G., Bargossi, G.M., Bondi, M., 1992. A new mantle xenolith locality in southern Ethiopia. Mineral. Mag. 56, 422–425.

Nickel, K.G., Green, D.H., 1985. Empirical geothermobarometry for garnet peridotites and implications for the nature of the lithosphere, kimberlites and diamonds. Earth Planet. Sci. Lett. 73, 158–170.

Pasyanos, M., Nyblade, A., 2007. A top to bottom lithospheric study of Africa and Arabia. Tectonophysics 444, 27–44.

Ryan, W.B.F., Carbotte, S.M., Coplan, J.O., 2009. Global Multi-Resolution Topography synthesis. Geochem. Geophys. Geosyst. 10, Q03014. http://dx.doi.org/10.1029/2008GC002332.

Rychert, C.A., Hammond, J.O.S., Harmon, N., Michael Kendall, J., Keir, D., Ebinger, C., et al., 2012. Volcanism in the Afar Rift sustained by decompression melting with minimal plume influence. Nat. Geosci. 5, 406–409.

Shinjo, R., Chekol, T., Meshesha, D., Itaya, T., Tatsumi, Y., 2011. Geochemistry and geochronology of the mafic lavas from the southeastern Ethiopian rift (the East African Rift System): assessment of models on magma sources, plume–lithosphere interaction and plume evolution. Contrib. Mineral. Petrol. 162, 209–230.

Soustelle, V., Tommasi, A., Bodinier, J.L., Vauchez, A., Garrido, C.J.M., 2009. Deformation and reactive melt transport in the mantle lithosphere above a partial melting domain (Ronda peridotite massif, Spain). J. Petrol. 50, 1235–1266.

Soustelle, V., Tommasi, A., Demouchy, S., Ionov, D., 2010. Deformation and fluid–rock interactions in the supra-subduction mantle: microstructures and water contents in peridotite xenoliths from the Avacha Volcano, Kamchatka. J. Petrol. 51, 363–394.

Stamps, D., Flesch, L., Calais, E., Ghosh, A., 2014. Current kinematics and dynamics of Africa and the East African rift system. J. Geophys. Res. 119, 5161–5186.

Takei, Y., Holtzman, B.K., 2009. Viscous constitutive relations of solid–liquid composites in terms of grain boundary contiguity: 1. Grain boundary diffusion control model. J. Geophys. Res. 114, B06205. http://dx.doi.org/10.01029/02008JB005850.

Tommasi, A., Vauchez, A., 2015. Heterogeneity and anisotropy in the lithospheric mantle. Tectonophysics 661, 11–37.

Vollmer, F.W., 1990. An application of eigenvalue methods to structural domain analysis. Geol. Soc. Am. Bull. 102, 786–791.

Walker, K.T., Nyblade, A.A., Klemperer, S.L., Bokelmann, G.H.R., Owens, J.T., 2004. On the relationship between extension and anisotropy: constraints from shear-wave splitting across the East African Plateau. J. Geophys. Res. 109, B08302.

Weeraratne, D.S., Forsyth, D.W., Fischer, K.M., Nyblade, A.A., 2003. Evidence for an upper mantle plume beneath the Tanzanian craton from Rayleigh wave tomography. J. Geophys. Res. Solid Earth 1978–2012, 108.

Wölbern, I., Rümpker, G., Link, K., Sodoudi, F., 2012. Melt infiltration of the lower lithosphere beneath the Tanzania craton and the Albertine rift inferred from S receiver functions. Geochem. Geophys. Geosyst. 13.

Woldegabriel, G., Yemane, T., Suwa, G., White, T., Asfaw, B., 1991. Age of volcanism and rifting in the Burji-Soyama area, Amaro Horst, southern main Ethiopian Rift: geochronological and biochronologic data. J. Afr. Earth Sci. 13, 437–447.